A processive rotary mechanism couples substrate unfolding and proteolysis in the ClpXP degradation machinery

Zev A. Ripstein[1,2†], Siavash Vahidi[1,2,3,4†], Walid A. Houry[1,4], John L. Rubinstein[1,2,5] and Lewis E. Kay[1,2,3,4]

[1]Department of Biochemistry, University of Toronto, Toronto, Ontario, M5S 1A8, Canada.

[2]The Hospital for Sick Children Research Institute, Toronto, Ontario, M5G 0A4, Canada.

[3]Departments of Molecular Genetics, University of Toronto, Toronto, Ontario, M5S 1A8, Canada.

[4]Department of Chemistry, University of Toronto, Toronto, Ontario, M5S 3H6, Canada.

[5]Department of Medical Biophysics, University of Toronto, Toronto, Ontario, M5G 1L7, Canada.

† Z.A.R and S.V contributed equally to this work

Abstract

The ClpXP degradation machine consists of a hexameric AAA+ unfoldase (ClpX) and a pair of heptameric serine protease rings (ClpP) that unfold, translocate, and subsequently degrade client proteins. ClpXP is an important target for drug development against infectious diseases. Although structures are available for isolated ClpX and ClpP rings, it remains unknown how symmetry mismatched ClpX and ClpP work in tandem for processive substrate translocation into the ClpP proteolytic chamber. Here we present cryo-EM structures of the substrate-bound ClpXP complex from *Neisseria meningitidis* at 2.3 to 3.3 Å resolution. The structures allow development of a model in which the cyclical hydrolysis of ATP is coupled to concerted motions of ClpX loops that lead to directional substrate translocation and ClpX rotation relative to ClpP. Our data add to the growing body of evidence that AAA+ molecular machines generate translocating forces by a common mechanism.

Introduction

Protein degradation plays a central role in cellular physiology, regulating the timing of cell division, controlling stress responses, and ensuring the timely removal of damaged or aberrantly folded proteins (1, 2). The ClpXP system is essential for protein degradation in bacteria and mitochondria and is a key regulator of cellular homeostasis, pathogenesis, and intracellular parasitism (3–5). It also serves as a model for understanding the structure and function of other ATP-dependant proteolytic systems. The ClpXP holoenzyme is composed of a hexameric AAA+ (ATPases Associated with diverse cellular Activities) unfoldase (ClpX) and a tetradecameric serine protease consisting of two heptameric rings (ClpP). Together, the ClpXP complex acts to unfold and degrade protein substrates (Figure 1A) (6). ClpXP is essential in bacteria, and consequently small molecules that disrupt either the protease (e.g. β-lactones (7), phenyl esters (8, 9)) or AAA+ unfoldase (e.g. ecumicin (10), lassomycin (11), rufomycin (12), dihydrothiazepines (13)), or mimic the interaction between the two (e.g. acyldepsipeptides [ADEPs] (14–16)) can kill cells, establishing ClpXP as a target for novel therapeutics against a range of different infectious diseases and cancers (17–21).

X-ray crystallographic studies of ClpP alone reveal a barrel-like structure with the protease rings stacked coaxially to form an enclosed degradation chamber that sequesters the fourteen Ser-His-Asp catalytic triads (22, 23), akin to the 20S proteasome (24, 25). Early negative-stain electron microscopy showed that one or two ClpX particles can bind co-axially to ClpP, creating a continuous central channel for substrates from ClpX to the degradation chamber of ClpP (26–28). Biochemical and X-ray crystallographic studies show that the axial entrances to the degradation chamber are gated by flexible N-terminal loops of ClpP that open upon the binding of ClpX or ADEPs, allowing substrates into the degradation chamber (29–31). Binding

53 of ClpX and ClpP is mediated by loops containing an Ile-Gly-Phe motif (IGF loops) on ClpX
54 that dock into hydrophobic pockets on the apical interfaces of ClpP subunit pairs (32–34). N-
55 terminal loops on ClpP also transiently interact with ClpX (33, 35, 36). However, the precise
56 nature of these interactions and how they allow coordination of the activities of ClpX and ClpP
57 remains unclear.

58 ClpX uses energy released by ATP hydrolysis to create a pulling force that unravels
59 folded protein domains for translocation into the degradation chamber of ClpP (6). This
60 unfolding activity relies on a series of highly conserved loops in ClpX. These loops include the
61 'RKH' loops that surround the ClpX entrance pore and recognize substrates for proteolysis (37),
62 and a pair of "pore loops" in each protomer, termed pore-1 loop (GYVG motif) and pore-2 loop
63 (RDV motif) (Figure 1 – figure supplement 1A) that line the axial channel of the ClpX ring (38).
64 Bulky aromatic and aliphatic side chains of the pore loops transmit the pulling force to the
65 substrate, leading to its unfolding. While the mechanism by which some AAA+ ATPases convert
66 the chemical energy of ATP into a mechanical force that unfolds substrates was established
67 recently (39–44), and structures of ClpP and ClpX in isolation have been determined (45–48),
68 the absence of structures showing ClpXP in the process of unfolding substrate has prevented an
69 understanding of the conformational changes that are necessary for substrate engagement,
70 unfolding, and translocation in this system. ClpXP must undergo hundreds of ATP hydrolysis
71 events to unfold and degrade a single protein, likely via a process involving hydrolysis of one
72 nucleotide at a time, but the lack of structural information for a ClpXP holoenzyme has limited
73 understanding of how unfolding and degradation are coupled. For example, it is not clear how
74 the symmetry mismatch (49–51) between the pseudo-symmetric hexameric ClpX and the seven-
75 fold symmetric ClpP affects both the binding and interaction of these two components.

76 Here we present cryo-EM structures of the ClpXP holoenzyme from the gram-negative
77 pathogen *Neisseria meningitidis* engaged with a protein substrate. The ClpXP portion of the
78 structure is at 2.3 to 3.3 Å resolution, allowing construction of a nearly complete atomic model
79 of the complex. Our findings show how ClpX grips and translocates substrates into the
80 degradation chamber through a cycle of ATP hydrolysis events involving both concerted motions
81 of pore loops along the substrate, as well as motions of ClpX on the apical surface of ClpP. The
82 data lead to a model for interactions between symmetry-mismatched ClpX and ClpP that enable
83 continuous degradation of substrates as ClpX rotates relative to ClpP.
84

85 **Results**

86 **ATP-dependent binding and degradation of GFP-SsrA by ClpXP**

87 ClpX and ClpP from *N. meningitidis* were expressed separately in *E. coli* before purification with
88 metal affinity chromatography and size exclusion chromatography (SEC). Degradation assays
89 using green fluorescent protein bearing an eleven-residue SsrA tag (GFP-SsrA) (43) were
90 performed to ensure that the heterologously expressed *N. meningitidis* (Nm) ClpX and ClpP
91 proteins, when mixed, have the well-established activity of the ClpXP holoenzyme. The presence
92 of ClpP or ClpX alone led to no loss of GFP-SsrA fluorescence relative to background bleaching
93 in the GFP-alone control assay. ClpX, ClpP, and ATP were all necessary to degrade GFP-SsrA
94 (Figure 1B), confirming that degradation of GFP-SsrA by ClpXP is ATP-dependent. As shown
95 below and in previous work (33, 52–54), the presence of MgATP is required for tight binding
96 between ClpX and ClpP. Therefore, for further structural studies, an E185Q Walker B mutant of
97 NmClpX (ClpX-WB) was used to slow ATP hydrolysis and prolong the lifetime of the ClpXP
98 complex. SEC was performed to probe the oligomeric state of each component and the formation

99 of the holoenzyme, confirming that ClpP behaves as an oligomeric species consistent with its
100 well-known tetradecameric architecture (Figure 1C – blue trace). ClpX-WB eluted as a hexamer
101 in the presence of 2 mM MgATP (Figure 1C – green trace). Incubation of ClpX-WB and ClpP in
102 the presence of MgATP resulted in a pair of higher molecular weight SEC peaks that contain
103 both ClpX and ClpP (Figure 1C – red trace and SDS-PAGE gel insert), presumably
104 corresponding to singly and doubly capped ClpXP complexes, that show that the ClpX:ClpP
105 complex can be readily reconstituted *in vitro* with the *N. meningitidis* enzyme.

106 To isolate a substrate-bound holoenzyme, ClpXP was incubated with GFP-SsrA in the
107 presence of MgATP. SEC fractions corresponding to doubly capped ClpXP bound to GFP-SsrA
108 (Figure 1–figure supplement 1B - denoted with a *) were applied to specimen grids and vitrified
109 for cryo-EM analysis. Visual inspection of the micrographs, as well as 2D classification of
110 particle images, showed doubly capped complexes (Figure 1-figure supplement 2). However, 2D
111 classification showed multiple classes where the two ClpX rings have lower density than the
112 ClpP region, and other classes with one ClpX ring having strong density and the other having
113 weak density. An *ab initio* 3D map showed ClpP along with strong density for one ClpX ring
114 and only weak and fragmented density for the other (Figure 1–figure supplement 2C). Inspection
115 of the map revealed that the ClpX ring is offset and tilted relative to the ClpP symmetry axis (Fig
116 1D, Video 1). The poor density for the second ClpX hexamer is likely due to the lack of
117 correlation between binding offsets of the two ClpX rings which leads to incoherent averaging of
118 one of the ClpX rings in the map. Refinement of the intact map led to an overall resolution of 2.8
119 Å (Figure 1–figure supplement 2C), however the density for the better-resolved ClpX ring
120 remained fragmented. Further local refinement and classification in cryoSPARC (55) improved
121 the density for ClpX and revealed two distinct conformations, at 3.3 Å and 2.9 Å resolution

122 (Figure 1–figure supplement 2), hereafter referred to as Conformations A and B, respectively.
123 Focused refinement of ClpP with D7 symmetry applied led to a map at 2.3 Å resolution (Figure
124 1–figure supplement 2).

125 **Overall architecture of NmClpXP**

126 Atomic models built into the cryo-EM maps showed that in both Conformations A and B, ClpX
127 is positioned with an offset and is tilted relative to the seven-fold symmetry axis of ClpP (Figure
128 1D, Video 1). Nevertheless, a continuous channel for substrate spans the ClpX and ClpP rings.
129 ClpP is in its active extended conformation (56), and closely resembles a published ADEP-bound
130 crystal structure with an all atom RMSD of 1.04 Å (56). Even though the full-length constructs
131 of ClpX included the zinc binding domains (residues 1-62), no density was found for these
132 domains in either conformation, likely due to their flexibility.

133 Conformations A and B of ClpX both contained additional density along their axial
134 channels, adjacent to the pore loops, likely from the GFP-SsrA substrate that co-eluted with
135 ClpXP from the SEC column (Figure 1E and 1F - orange) (Figure 1 – Figure Supplement 1B).
136 The substrate enters ClpX at an angle of ~15° relative to the ClpP symmetry axis, and is gripped
137 by five of the six ClpX protomers arranged in a right-handed spiral, akin to other AAA+
138 ATPases in their substrate-bound conformations (39–44). The sixth protomer forms a disengaged
139 "seam" that bridges protomers at the beginning and end of the spiral. In the description that
140 follows we have labeled the protomers X1 through X6 corresponding to their position in the
141 spiral (Figure 1F), and consider the configuration in which X1 is the disengaged "seam"
142 protomer of Conformation A.

143 The main differences between Conformations A and B are within the protomer that
144 adopts the bridging seam position, and where the seam is located relative to ClpP. In

145 Conformation A, protomer X1 is disengaged from substrate and in the seam position (Figure 1F
146 left - dark blue) while in Conformation B protomer X6 is disengaged from substrate and in the
147 seam position (Figure 1F right - yellow). However, these two seam positions are not equivalent:
148 in Conformation A the seam is further from the apical surface of ClpP in what we designate as
149 the "upper seam" (US) position (Figure 1D,F - dark blue), while in Conformation B, the seam is
150 closer to ClpP in the "lower seam" (LS) position (Figure 1D,F - yellow).

151 **The symmetry-mismatched interaction interface between ClpX and ClpP**

152 ***ClpX IGF Loops:*** In both Conformations A and B of ClpXP, there is clear density for most of
153 the IGF loops that extend from the ClpX ring towards the apical surface of ClpP (Figure 2A). In
154 Conformation A, clear density is observed for only five of the six IGF loops, with weak density
155 belonging to the IGF loop of the X6 protomer (white dotted line in Figure 2B left; Figure 2-
156 figure supplement 1). In Conformation B, the density of the X6 IGF loop is significantly stronger
157 than in Conformation A, so that all six of the IGF loops are accounted for (residues 264-274,
158 Figure 2B, right; Figure 2C; Figure 2-figure supplement 1), with the loops binding six of the
159 seven pockets on ClpP. In both Conformations A and B, the empty ClpP binding pocket is
160 located between the X5 and X6 protomers of ClpX (Figure 2B). The lack of density for the IGF
161 loop belonging to protomer X6 in Conformation A (Figure 2-figure supplement 1) is likely due
162 to conformational flexibility and sub-stoichiometric binding of this IGF loop into the ClpP
163 binding pocket.

164 All six IGF loops in ClpX adopt different configurations in Conformations A and B
165 (Figure 2-figure supplement 1). The ClpX residues immediately following where the IGF loops
166 contact ClpP (residues 275-280) show weak or no density, likely indicating flexibility. This
167 property allows the IGF loops to accommodate movement of the ClpX protomers relative to

168 ClpP (Figure 2D-F), analogous to a set of springs. For instance, in Conformation A the X1
169 protomer is closer to the ClpP surface than in Conformation B and its IGF loop is thus compact
170 in this state. In contrast, in Conformation B the loop is fully extended, allowing the X1 protomer
171 to reach ~7 Å towards the top of the spiral to engage the substrate (Figure 2F; Figure 2-figure
172 supplement 1). In this way the flexibility of the IGF loops accommodates the spiral arrangement
173 of ClpX necessary to bind and unfold substrate, while maintaining contact with the planar ring of
174 ClpP. Additionally, the IGF loops allow the X2 protomer to move laterally away from the ClpP
175 pore while the X4 and X5 protomers move toward it to form a structure in which the ClpP and
176 ClpX rings are displaced with respect to each other (Figure 2D-red arrow; Figure 2E).

177 ***ClpP N-terminal Gates:*** Degradation assays (31, 35, 57–59) have shown that ClpX can open the
178 N-terminal gates of ClpP, and indeed in both Conformations A and B the gates are in the "up"
179 state, forming ordered β-hairpins (Figure 2G; Figure 2-figure supplement 2). These β-hairpins
180 closely resemble the conformation seen in the ADEP-bound structures of NmClpP (56) and are
181 notably different from the disordered conformations observed in NmClpP when it is not bound to
182 either ClpX or ADEP (Figure 2–figure supplement 2B). By forming ordered gates, ClpX binding
183 creates a wide entrance pore with a diameter of ~23 Å for substrates to pass through into the
184 ClpP degradation chamber (Figure 2G, left; Figure 2–figure supplement 2). While it has long
185 been suspected that the activating mechanism of ADEPs involves a disorder-to-order transition
186 of these gates (30), this observation provides direct evidence that ClpX creates the same effect.

187 In both Conformations A and B, the rigidification of the ClpP N-terminal gates varies
188 substantially between protomers. At one extreme, the N-terminal residues of the ClpP protomer
189 that is not bound to an IGF loop have the weakest density, appearing to possess the most
190 flexibility at the top of the β-hairpin (Figure 2G center; Figure 2-figure supplement 2E). In

191 contrast, the N-terminal residues of the ClpP protomer proximal to the X5 ClpX protomer, are
192 held rigidly through contacts with the ATPase (Figure 2G right). This interaction is mediated by
193 a pair of α-helices from protomer X5 (residues 254-262 and 291-296) adjacent to the IGF loop,
194 and by another X5 α-helix that precedes the pore-2 loop (residues 186-192). These three α-
195 helices stabilize the β-hairpin structure of the ClpP N-terminal residues by interacting with
196 Arg17 at the top of the hairpin (Figure 2E inset). These interactions are unique for the X5
197 protomer due to the lateral displacement of the ClpX ring relative to the axial pore of ClpP
198 (Figure 2A), with the X2 protomer shifted furthest from the pore while the X5 protomer is pulled
199 overtop of the pore (Figure 2D&F). Even without interacting directly with ClpX, the remaining
200 five ClpP protomers have nearly rigid N-terminal gates, with reduced density only for residues
201 located in the turn of the β-hairpin that likely reflects increased flexibility in this region (Figure
202 2-figure supplement 2F). Gate rigidification therefore appears to be mediated by an allosteric
203 effect when IGF loops engage their respective ClpP binding pockets, akin to the effect observed
204 upon ADEP binding (15, 30). In the ClpXP complex with substrate bound, only a single ClpX
205 protomer (X5) interacts directly with a single ClpP gate at any given time. The mechanism of
206 substrate translocation described below involves movement of the ClpX ring on the apical
207 surface of ClpP, with each ClpX protomer forming contacts with a ClpP gate as translocation
208 proceeds.

209 **Substrate Engagement by ClpX**

210 ClpX fits neatly into the emerging consensus for how AAA+ unfoldases engage substrate (39–
211 43). In both Conformations A and B, five of the six pore-1 loops of ClpX interact tightly with the
212 substrate backbone, with Tyr153 forming the majority of the interface (Figure 3A&B). These
213 protomers generate a right-handed spiral that wraps around an 8 to 10 residue stretch of the

214 substrate along the central channel of ClpX (Figure 3C&D). In Conformation A, the X1 pore-1
215 loop in the US orientation is disengaged, with the X2 protomer at the top of the spiral. As the
216 spiral continues downwards, protomers X3, X4, and X5 make contacts with the substrate. The
217 spiral terminates with the X6 pore-1 loop that is engaged with the substrate closest to the ClpP
218 apical surface (Figure 3C). In Conformation B, the X6 pore-1 loop is disengaged (LS
219 orientation), while the X1 pore-1 loop engages a new section of substrate (Figure 3D) and the X5
220 protomer is now located closest to the ClpP surface. When transitioning between substrate-
221 engaged and disengaged states, the X6 pore-1 loop undergoes a large conformational change
222 (Figure 3E). As it disengages the substrate the "lasso" fold (Figure 3E, left) that allows Tyr153
223 and Val154 of pore 1 to point towards the substrate is replaced by a short α-helix immediately
224 following the GYVG motif of the loop.

225 Interestingly, the X1 and X5 protomers make additional contacts with the substrate in
226 Conformation B. Whereas all of the pore-2 loops from the other five protomers are radially
227 removed and disengaged from the substrate, the X1 protomer extends its pore-2 loop residues
228 Ile198 and Thr199 to engage the substrate at a position three or four residues down the substrate
229 chain from where its pore-1 loop binds (Figure 3D&F). The RKH loops, located at the top of the
230 ClpX ring (Figure 3–figure supplement 1), are highly conserved motifs among the ClpX family
231 of AAA+ unfoldases and are known to contribute to substrate recognition (60–62). In
232 Conformation B only the RKH loop of X5 directly engages substrate, with its His230 residue
233 interacting at a position three or four residues up the substrate chain from where its pore-1 loop
234 binds (Figure 3D&F). In order to contact substrate at this position the RKH loop of the X5
235 protomer rearranges to point toward ClpP (Figure 3F), in contrast to the other RKH loops which
236 point away from the axial channel of ClpX (Figure 3-figure supplement 1). These five RKH

237 loops are located away from the substrate, and have weaker density in the maps, likely indicating
238 flexibility.

239 **Nucleotide State and Cycling in ClpX**

240 The cryo-EM maps allowed unambiguous identification of the nucleotide bound to each ClpX
241 protomer. In Conformation A, there is strong density for ATP and a magnesium cofactor in
242 protomers X2, X3, X4, and X5, while the X1 and X6 protomers are ADP loaded, with no density
243 for either the γ-phosphate or magnesium (Figure 4A,4C). As in both the classic and HCLR clades
244 of AAA+ ATPases (39–43), the orientation between the large and the small AAA+ domains of
245 ClpX changes considerably depending on the nucleotide state. In Conformation A, both the X1
246 and X6 protomers adopt conformations that allow the X1 protomer to move away from the pore
247 in the US position (Figure 4-figure supplement 1) and there is reduced surface area buried
248 between X1 and its neighboring protomers X2 and X6. In agreement with this finding, the local
249 resolution in the cryo-EM maps (Figure 4-figure supplement 2) shows that the X1 protomer in
250 the US position is significantly more flexible than the other protomers. In Conformation B only
251 the X6 protomer is ADP-bound. The X1, X2, X3, X4, and X5 protomers are ATP-bound with
252 clear density for the γ-phosphate and the magnesium cofactor (Fig 4B and D). Interestingly, the
253 X5 protomer adopts a unique orientation between its large domain and small domain compared
254 to the other ATP-bound protomers in order to accommodate the translation of the X6 protomer
255 away from the substrate translocation channel into the LS position (Figure 4B orange box; Figure
256 4-figure supplement 1).

257 In Conformation A, the β- and γ-phosphates of the bound ATP are stabilized by
258 interactions with the sensor-II arginine (Arg369) of the same subunit and the arginine finger
259 (Arg306) from the adjacent clockwise protomer (Figure 4C). In the ADP-bound sites of the X1

260 and X6 protomers, both arginines have moved away, allowing for a more open nucleotide
261 binding pocket (Figure 4C). In contrast, in Conformation B both the sensor-II arginine and the
262 arginine finger contact the β and γ-phosphates in only four of the five ATP-bound protomers
263 (X1, X2, X3, and X4) (Figure 4D). In the ATP-bound X5 protomer (at the bottom of the spiral),
264 the adjacent X6 protomer and its arginine finger have pivoted away from the nucleotide into the
265 LS position, allowing the sensor-II arginine to move closer to the γ-phosphate of the bound ATP.
266 In addition, the Walker B motif moves closer to ATP presumably to prime this site for ATP
267 hydrolysis. Notably, this key sensor II-priming motif in the primed nucleotide site has also been
268 reported for the Lon protease bound to substrate (42), a close relative in the HCLR clade of
269 AAA+ proteins.
270

271 **Discussion**

272 In this study we used cryo-EM to build atomic models of a ClpXP complex bound to a SsrA-
273 tagged GFP substrate. Structures of a variety of different AAA+ rings with substrates have
274 emerged in the past several years (39–43), providing a description of how these ATP-dependent
275 molecular machines unfold clients. In addition, methyl-TROSY NMR studies of a VAT-
276 substrate complex provided atomic-level insights into structural changes associated with the
277 client as it is pulled into the lumen of the unfoldase (63). Nevertheless, a detailed understanding
278 of how a pair of symmetry mismatched ClpP/ClpX rings can work in tandem to unfold,
279 translocate, and subsequently degrade substrates in a processive manner has remained elusive.
280 Our structural data suggest a translocation mechanism that can be explained in terms of a pair of
281 conformers, denoted as Conformations A and B here, that represent two steps along the substrate
282 translocation pathway (Figure 5A). To aid in the following discussion we have color-coded the

283 ClpX protomers and refer to them with their X1 - X6 labels. As we will discuss, each of these
284 protomers will cycle between all six protomer positions along the spiral, including, among
285 others, a state primed to hydrolyze ATP (denoted as ATP*) as well as the LS and US positions.
286 This cycling is linked to ATP hydrolysis, to the attachment position of ClpX pore-loops along
287 the substrate, and to the interaction of ClpX IGF loops with ClpP. We begin our discussion of the
288 unfolding/translocation cycle with the X1 protomer in Conformation A in the US position,
289 detached from substrate and bridging the lowest and highest positions of the ClpX spiral. Both
290 X1 and X6 protomers are ADP-bound, while the remaining protomers are in ATP-bound states.
291 In Conformation B, X1 moves to the highest position of the spiral with respect to substrate
292 (compare Figure 2F, top and bottom panels) simultaneously exchanging ADP for ATP in its
293 nucleotide binding pocket (Figure 5B). This transition brings X1 into close proximity with X2
294 and allows engagement of X1's pore loops with substrate. The X1 pore-l loop now sits at the top
295 of the spiral, two substrate residues above the X2 pore loop (Figure 5A&B), thereby
296 translocating additional residues of substrate into the unfoldase. This transition also leads to
297 release of substrate by X6, which pivots away from the central pore to adopt the LS position
298 (second ring, Figure 5A). ATP hydrolysis and phosphate release by X5, which was in the ATP-
299 hydrolysis primed ATP* state, restores the ClpX spiral back to the Conformation A state, (third
300 ring of the four in Figure 5A), with X6 now assuming the US position. The complex is thus reset
301 so that it can take another step along the substrate during the next A to B transition (third ring to
302 fourth ring in Figure 5A). The cumulative effect of these transitions is a cycling of ClpX
303 protomers through different positions on the spiral (Figure 5A&B). For example, the protomer
304 initially in the US position (X1 in our discussion) will, with each step, move along the spiral
305 such that it transitions from the US position to the top of the spiral (Conformation B) and then

306 successively moving to lower spiral positions, through the ATP* state and finally the LS
307 position, as substrate is translocated. Each Conformation A→Conformation B→Conformation A
308 step results in the exchange of ADP for ATP and a single ATP hydrolysis event. Continuous
309 repetition of these steps leads to a processive "hand-over-hand" translocation of substrate
310 through the axial pore of ClpX into ClpP (Illustrated in Video 2).

311 The sequential hydrolysis of ATP at the ATP* position results in unidirectional substrate
312 translocation and movement of pore loops along the substrate (Figure 5B), with the counter
313 clockwise hydrolysis cycle translating into a repeated downward pulling force on the substrate.
314 Both the sequential hydrolysis of ATP as well as the "hand-over-hand" substrate pulling model
315 appear to be conserved for AAA+ unfoldases (39–43).

316 The cycle described above, in which each protomer eventually adopts all positions in the
317 spiral, has significant implications for how the IGF loops interact with the ClpP binding pockets.
318 If the spiral position of each ClpX protomer was independent of IGF binding, alignment of the
319 asymmetric ClpX spiral would lead to averaging of the IGF loops into all the pockets of ClpP
320 during cryo-EM map refinement. However, our structures clearly show an empty IGF pocket on
321 ClpP *only* between the ATP* and LS positions of Conformation B (Figure 2B), suggesting that
322 this pocket must undergo a "cycle" as well (Figure 5C). Thus, following ATP hydrolysis and
323 phosphate release, the IGF loop of the protomer in the ATP* position (X5 initially) must leave
324 its engaged pocket and move to bind the adjacent empty site on ClpP (red arrows in Figure 5C),
325 as the complex transitions back to Conformation A (third ring in Figure 5A). In this state, the
326 IGF loop appears not to have assumed a structure that allows for tight binding as only weak
327 density is observed for it in EM maps. In contrast, strong binding is observed for this loop in
328 Conformation B (Figure 4-figure supplement 1). Consistent with this model, the IGF loop of the

329 X5 protomer has an "extended/stretched" structure in the ATP* position of Conformation B
330 (Figure 2F), which likely causes strain and facilitates loop release and subsequent binding to the
331 corresponding site on the adjacent ClpP protomer (Figure 5C). After seven IGF loop release and
332 reengagement events, accompanied by seven ATP hydrolysis steps, the 'empty' ClpP binding
333 site makes a complete cycle, returning to its starting position (Figure 5C). The accompanying
334 motion of ClpX on the apical surface of ClpP for a given IGF loop transition is complex and
335 subtle, yet seven of these transitions lead to a net 60° rotation of ClpX with respect to ClpP (note
336 the positions of the purple ClpX protomer in the first and seventh panels in Figure 5D; Video 3).
337 The model described above is the simplest one that is consistent with our data. More complicated
338 models can be envisioned. For example, if each upward step of a ClpX protomer was not coupled
339 to IGF loop displacements, or relative motion of ClpX on the apical surface of ClpP, additional
340 states would have to be invoked, for which no experimental data has been observed.

341 During preparation of this manuscript two preprint manuscripts reported structures of
342 ClpXP from *L. monocytogenes* (64) and from *E. coli* (65), with ClpX resolutions ranging from
343 3.9 to 6 Å. While density maps and atomic models are not available for direct comparison with
344 the NmClpXP, a few important similarities and differences are notable. In all species, the ClpX
345 ring appears to adopt a similar offset relative to the symmetry axis of ClpP, indicating that the
346 general architecture of the ClpXP machinery is conserved. Notably, however, the N-terminal
347 apical loops of *L. monocytogenes* ClpP are not rigidified upon ClpX binding (64), in contrast to
348 the observation here that the gates rigidify upon binding to create a pore for substrate entry.
349 Additionally, substrate engagement is different between the ClpXP from *N. meningitidis*
350 described here and from *E. coli* (65). In the Conformation A seen with *N. meningitidis*, there is
351 no engagement of substrate by any of the six pore-2 or six RKH loops, while in Conformation B

352 only a single RKH loop and a single pore-2 loop contact substrate (Figure 3D&F). This
353 observation is in contrast to the recently reported *E. coli* ClpXP structures (65) in which
354 arginines located in the pore-2 loop from three to five different protomers (depending on the
355 structure), as well as multiple RKH loops, form major contacts with substrate. The differences in
356 these interactions may reflect the fact that while pore-1 loop motifs are critical for forming
357 interactions with client and in providing the force for translocation, additional contacts may
358 differ between species and may be necessary for recognition of degradation signals and for
359 substrate specificity.

360 Although in the ClpXP structures from *E. coli* (65) the ClpX ring adopts the same spiral
361 staircase arrangement observed in many AAA+ ATPases (39–43, 66, 67), strongly supporting
362 the "hand-over-hand" mechanism of substrate translocation, the authors of this work instead
363 posit a stochastic mechanism (65, 68) for the HCLR clade of ATPases based on the observation
364 of only a single bound ADP in their structures. In the stochastic model only a single protomer
365 pulls the substrate, via a state that has yet to be observed. Such a model, involving stochastic
366 nucleotide hydrolysis, appears inconsistent with the observations here and for the related Lon
367 protease (42) where two neighbouring protomers are bound with ADP. It also appears to be in
368 conflict with studies of the VAT AAA+ unfoldase (43) whereby nucleotide hydrolysis was
369 shown to occur in a cycle that could be disrupted through the substitution of a single hydrolysis-
370 impaired protomer into the ATPase ring. In contrast, the identification of two conformations in
371 the *N. meningitidis* enzyme and observations of the bound nucleotides in each ClpX protomer
372 leads to a simple model of cyclic hydrolysis that, in turn, results in unidirectional substrate
373 translocation. In this model, the substrate is always gripped by multiple protomers, with only a
374 single protomer disengaged as it traverses from the bottom to the top of the spiral. While unique

375 features will undoubtedly continue to emerge regarding subtle functional aspects of different
376 AAA+ unfoldases it is likely that the translocating forces generated by these molecular machines
377 are based on a common mechanism.

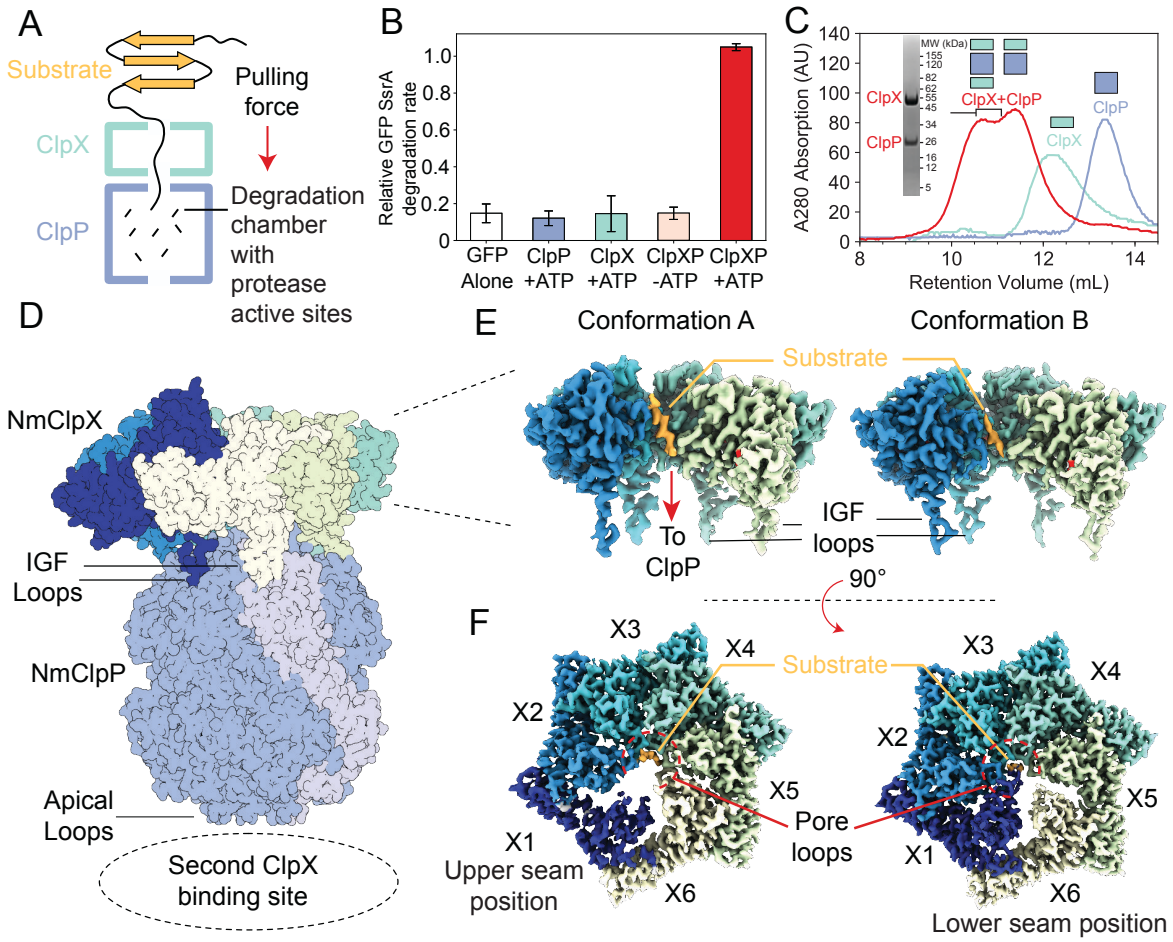

Figure 1. Functional and structural characterization of ClpXP from *N. meningitidis*. (A) Schematic representation of the ClpXP degradation machinery. The overall positions of the substrate (orange), ClpX unfoldase (green), and the ClpP protease (blue) are shown; (B) GFP-SsrA degradation by ClpXP is ATP-dependant. The degradation rate of GFP-SsrA is monitored by measuring loss of fluorescence. The components (ClpX, ClpP, ATP) included for each measurement are denoted on the plot. All measurements included GFP-SsrA and were performed in triplicate; (C) ClpXP complex formation monitored by size exclusion chromatography (SEC). SEC profiles of isolated ClpP (blue trace) and ClpX (green trace) are consistent with their expected molecular weights. SEC profile of a 2:1 $ClpX_6$:$ClpP_{14}$ mixture (red trace) incubated for 10 minutes in the presence of MgATP shows the formation of doubly- and singly-capped ClpXP complexes. The running buffer for all traces contained 2 mM MgATP. SDS-PAGE gel of SEC fractions shows that they contain both ClpP and ClpX; (D) Overall architecture of the ClpXP complex as established by cryo-EM. The ClpP double ring component is shown in dark blue, with the exception of a pair of opposing protomers shown in light blue shade to delineate the IGF loop binding site that is located at the interface between protomers. Cutaway side (E) and top (F) views of Conformations A and B of ClpX resulting from focused classification and local refinement. The IGF loops that bind to ClpP, and the presence of substrate (orange) in the axial channel of ClpX, are highlighted. Each of the ClpX protomers is labeled. In panel (F), the engagement of the substrate (orange) with five of the six pore loops is indicated (red semi-circle).

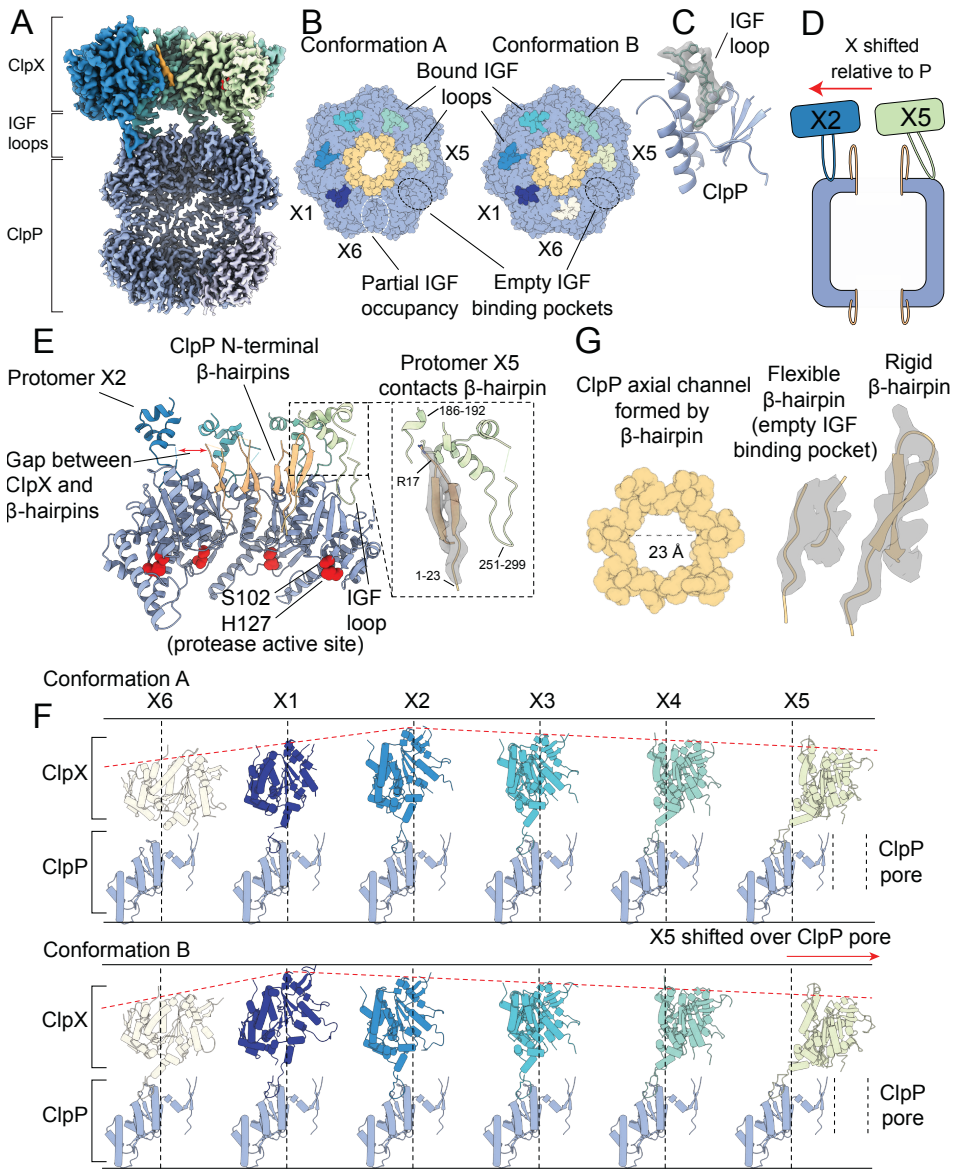

Figure 2: The interaction interface between ClpX and ClpP. Protomer X1 occupies the US position in Conformation A and protomer X6 the LS position in Conformation B. (A) Cutaway density map of the overall architecture of the ClpXP interaction interface. (B) Models for the ClpP apical surface and the ClpX IGF loops (residues 265-275). The empty IGF binding pocket (dotted oval) resides clockwise to the X5 protomer in both conformations. In Conformation A an IGF loop was not built into the map for protomer X6 due to weak loop density (yellow dotted line). (C) Model in map fit for an IGF loop (grey), surrounded by regions of ClpP comprising the IGF binding site (blue). (D) Interaction of the ClpP N-terminal gates with ClpX. The X2 protomer moves away from the gates, while the X5 protomer directly contacts the gate of the ClpP protomer to which its IGF loop is bound, shown schematically in (E). Inset shows the details of this interaction, with model in map fit for the ClpP β-hairpin. (F) Positions of ClpX protomers relative to ClpP. Images were generated by fitting all ClpP protomers to a common protomer and displaying the corresponding ClpX protomer. In both conformations ClpX adopts a spiral arrangement relative to ClpP (dotted red line). In Conformation A, the X2 protomer is located at the top of the spiral, while in Conformation B the X1 protomer occupies the top position, ~7 Å higher than its position in Conformation A. The ClpX protomers rotate and translate relative to ClpP; protomers X2 and X3 sit nearly atop their ClpP protomers, while X4 and especially X5 show large deviations from this position (vertical lines), with X5 sitting overtop the ClpP axial pore. (G) View down the channel formed by the N-terminal ClpP β-hairpins (left); density and models for the most flexible and rigid β-hairpins (center & right, respectively).

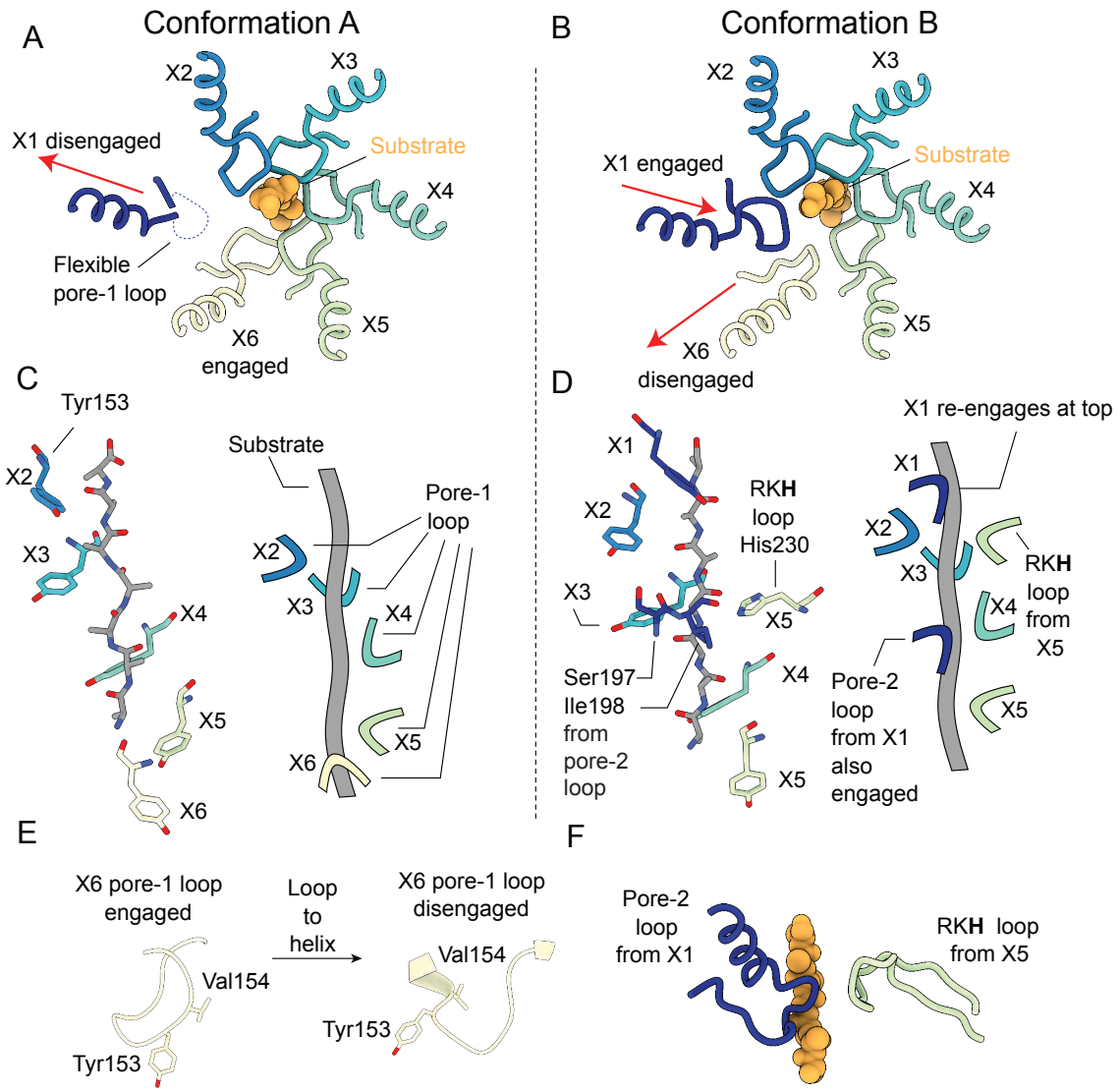

Figure 3. Substrate engagement by the ClpX pore loops. (A and B) Pore-1 loop residues grip the substrate, as observed in this view looking down the axial channel. The substrate is modelled as poly-Ala. (A) In Conformation A, the X1 protomer is disengaged from the substrate in the US position (red arrow) and shows noticeable flexibility in its pore-1 loop. (B) In Conformation B the X1 protomer contacts the substrate but the X6 protomer has disengaged into the LS position (red arrows). (C and D) Model of substrate and interacting residues, along with schematic, viewed perpendicular to the axial channel. (C) In Conformation A only the Tyr153 residue of the pore-1 loop makes significant contacts with the substrate; the 5 protomers (X2, X3, X4, X5, X6) form a downward spiral surrounding the backbone of the substrate chain, extending to the apical surface of ClpP. (D) In Conformation B, in addition to the five Tyr153 residues from the 5 gripping protomers (X1, X2, X3, X4, X5), more contacts are formed: Ser197 and Ile198 from the pore-2 loop of the X1 protomer and His230 from the RKH loop of the X5 protomer. (E) Substrate induced conformational changes of the X6 pore-1 loop upon releasing client. When the X6 protomer is substrate engaged its pore-1 loop forms a lasso like conformation, with Tyr153 and Val154 both pointing towards the axial channel (left). When disengaged, a part of the pore-1 loop becomes an α-helix, with Val154 and Tyr153 no longer pointing outwards (right). (F) Architecture of the additional contacts made by the pore-2 and RKH loops from the X1 and X5 protomers, respectively.

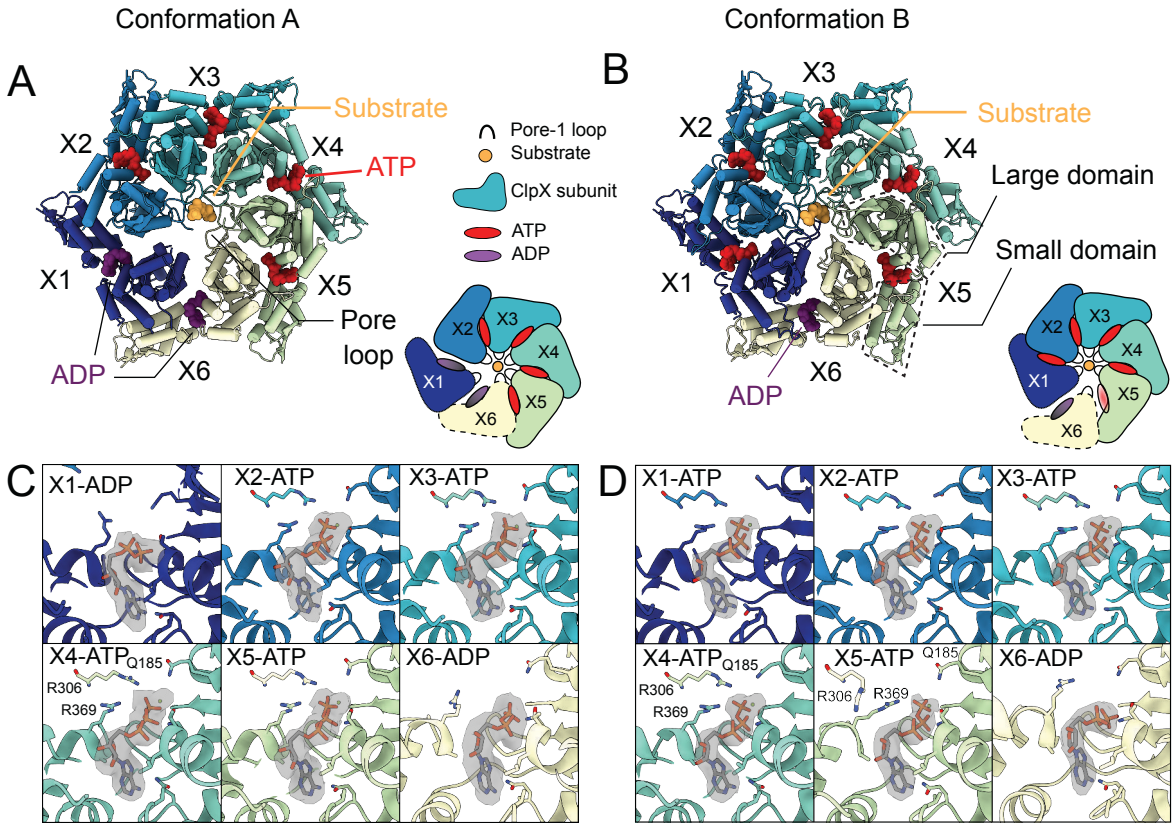

Figure 4. Nucleotide occupancy and interactions with ClpX. (A&B) Model of ClpX in conformations A and B, looking into the ClpX pore. Nucleotides are shown and color-coded, with ATP red and ADP purple, and bind between the large and small domains (boxed). Inset shows a schematic of the protomer positions and nucleotide occupancies. Conformation A has two bound ADP, in the X1 (dark blue, US in Conformation A in this representation) and X6 (yellow, LS in Conformation B in this representation) protomers, with the X1 protomer disengaged from the substrate and away from the axial pore (US position). In Conformation B only a single ADP is bound, protomer X1 is reengaged with substrate and X6 has disengaged. (C) Nucleotide binding sites of Conformation A, with key interacting residues shown along with the experimental density maps corresponding to bound nucleotide. In the ADP bound sites, both the arginine finger (R306) and the sensor-II arginine (R369) have moved away, while in the ATP bound sites they form close contacts with the β and γ-phosphates. (D) Nucleotide binding in Conformation B. As in Conformation A, R306 and R369 have moved away from the ADP, while in the X5 protomer only the arginine finger has moved away, while the sensor-II transitions closer to the γ-phosphate.

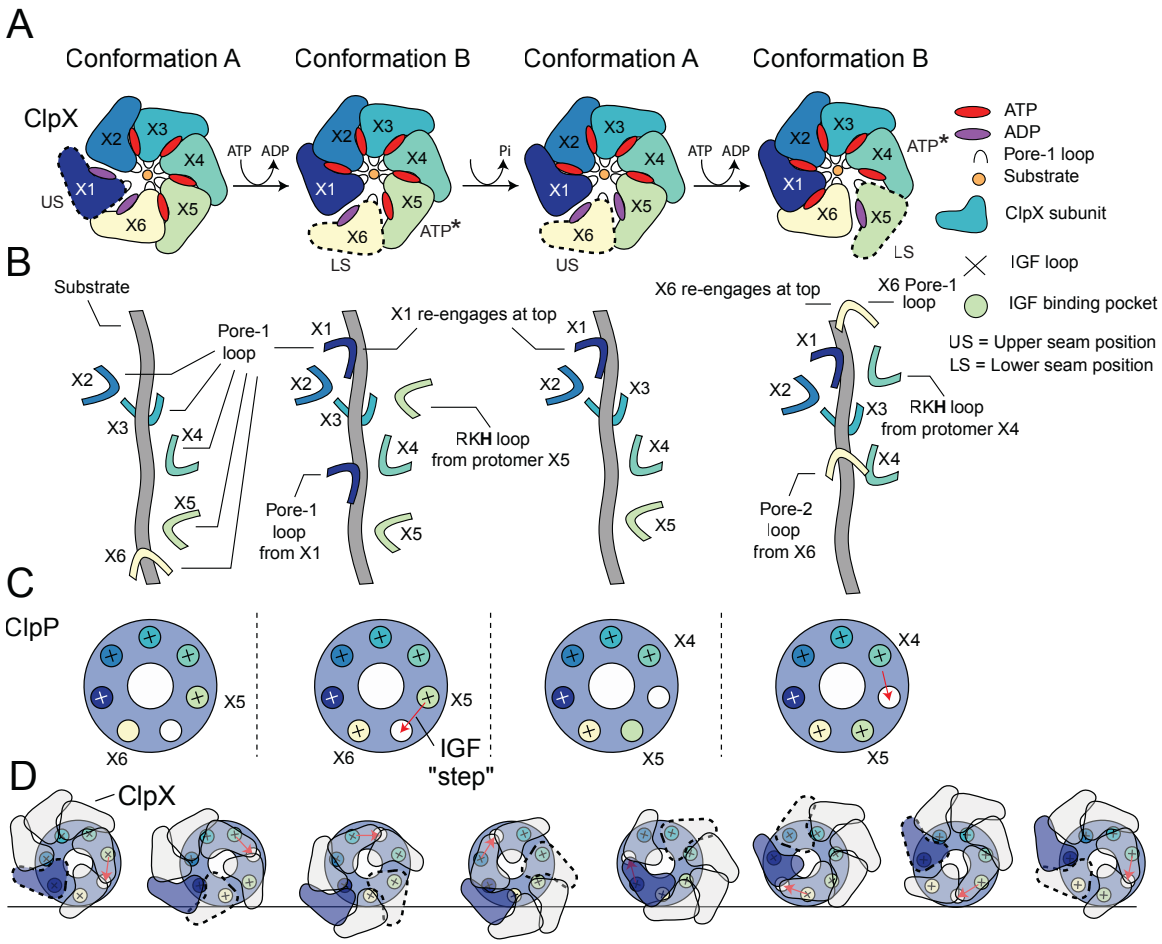

Figure 5. Translocation model for ClpXP. (A) Schematic of the ClpX nucleotide dependent conformational cycle. The transition from Conformation A to Conformation B is mediated through nucleotide exchange in the US position (1st to 2nd ring), with ATP hydrolysis and phosphate release in the ATP* position restoring the A conformation from the B state (2nd to 3rd ring) so that the cycle can repeat. In the new Conformation A (3rd ring), protomer X6 (yellow) adopts the US conformation and the X1 protomer (previous US) moves to the top of the spiral. In this way each protomer of the complex cycles through all positions as ATP is hydrolyzes in successively new ATP* protomer states, requiring the hydrolysis of seven ATPs. (B) Hand-over-hand mechanism of pore-loop mediated translocation. In the first A to B transition depicted in (A) X1 (US protomer) reengages at the top of the spiral and the LS pore 1 loop (X6 in Conformation B) disengages from the bottom of the spiral. As this is repeated the pore loops move "up" the substrate and pull it into the degradation chamber. (C) IGF loop movements accompanying the hand-over-hand movements of ClpX. Shown in the small circles are the seven IGF loop binding sites in ClpP with a '+' sign indicating engagement with an IGF loop of a given ClpX protomer. The binding sites are color coded according to the color of the protomer that interacts with the corresponding site. In conformation A, the IGF loop of X6 is unbound or only weakly bound, while in Conformation B it is bound. A new Conformation A is generated when the IGF loop from the ATP* protomer unbinds. It subsequently reengages with ClpP in a new Conformation B (third and fourth rings in Figure 5A). In this way the IGF loops "step" around the ClpP ring, with each complete rotation requiring the hydrolysis of seven ATPs. (D) Schematic of the ClpX-ClpP interactions during seven ATP hydrolysis steps that lead to a net rotation of ClpX protomers by 60°. Because of the six- to seven-fold symmetry mismatch a total of forty-two ATPs must be hydrolyzed to return the protomers back to their original starting positions in the cycle (*i.e.*, ring 1). Each of the seven ring structures corresponds to Conformation A, with the red arrows indicating the subsequent step of the IGF loop of the ATP* protomer along the cycle. The US protomer in each step is highlighted by the dashed trace.

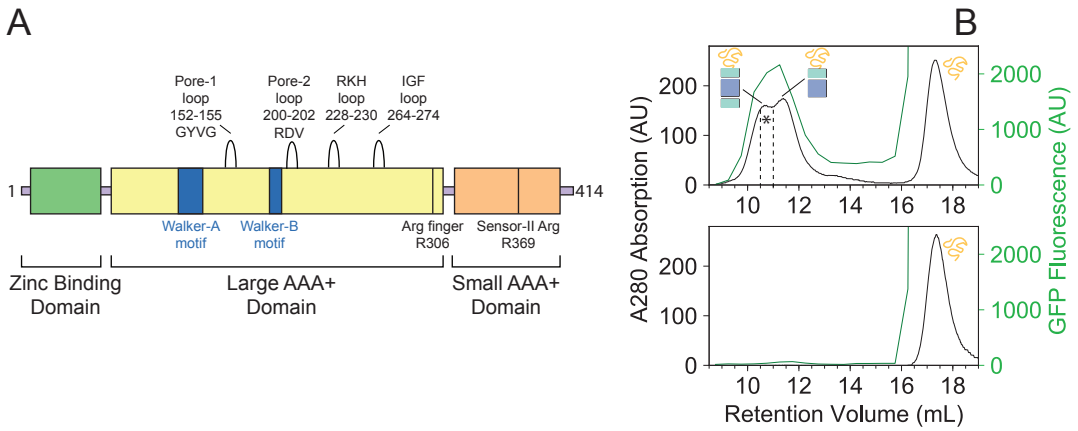

Figure 1 - Figure Supplement 1. (A) NmClpX primary sequence domain map. Important structural and functional motifs are denoted. (B) NmClpXP binds a SsrA-tagged GFP. SEC profiles for ClpXP incubated with GFP-SsrA (top panel) and GFP-SsrA alone (bottom panel) measured using absorbance at 280 nm (black trace) and GFP fluorescence (green trace - λ_{ex}:480nm, λ_{em}:508 nm). The region used for SDS PAGE analysis is highlighted by * (Figure 1C).

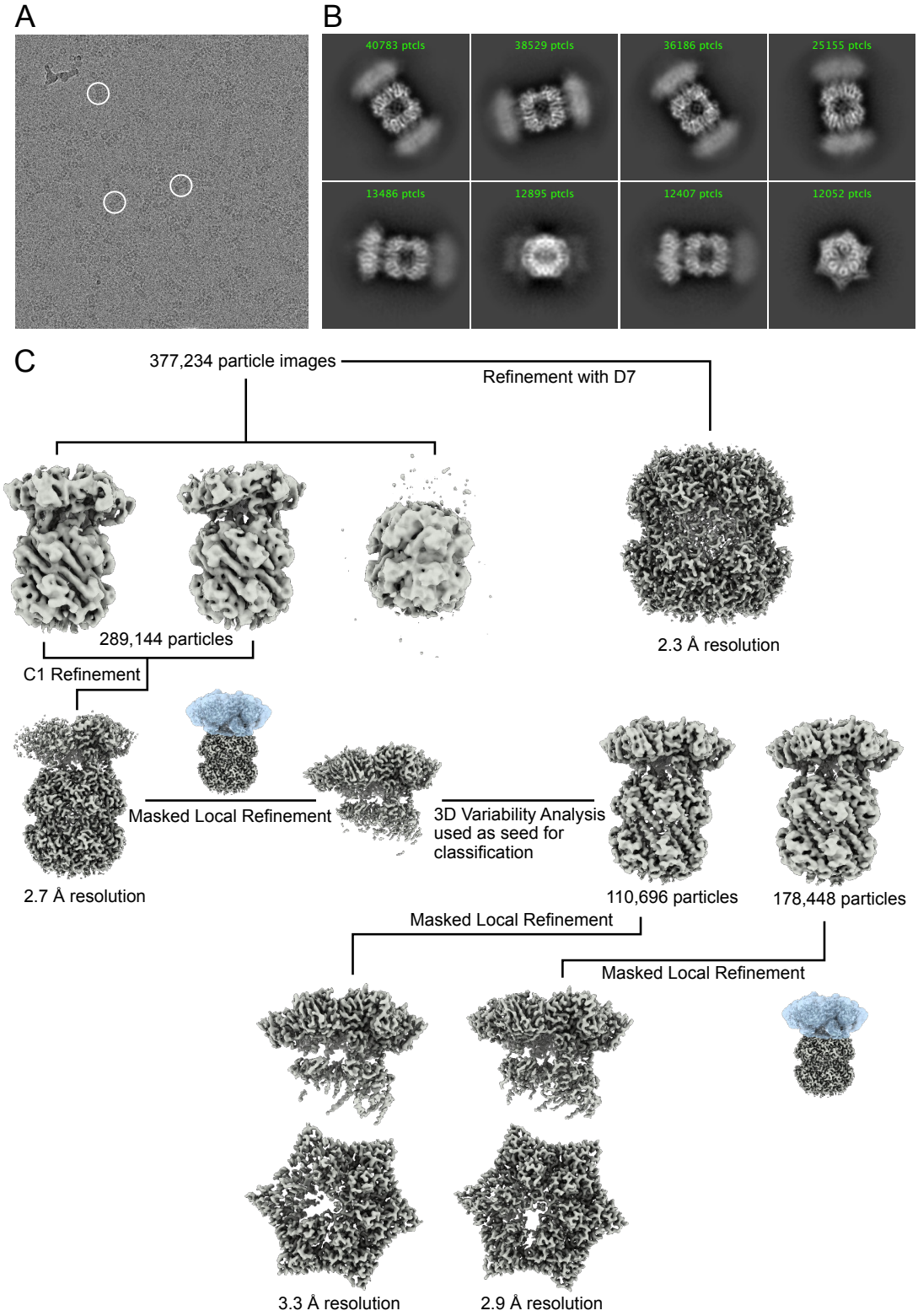

Figure 1 – Figure Supplement 2. Cryo-EM image processing. (A) Representative cryo-EM micrograph of NmClpXP bound to GFP-SsrA. Example complexes are circled in white. (B) Representative 2D class averages of NmClpXP with GFP-SsrA. (C) Image processing workflow used to obtain final maps.

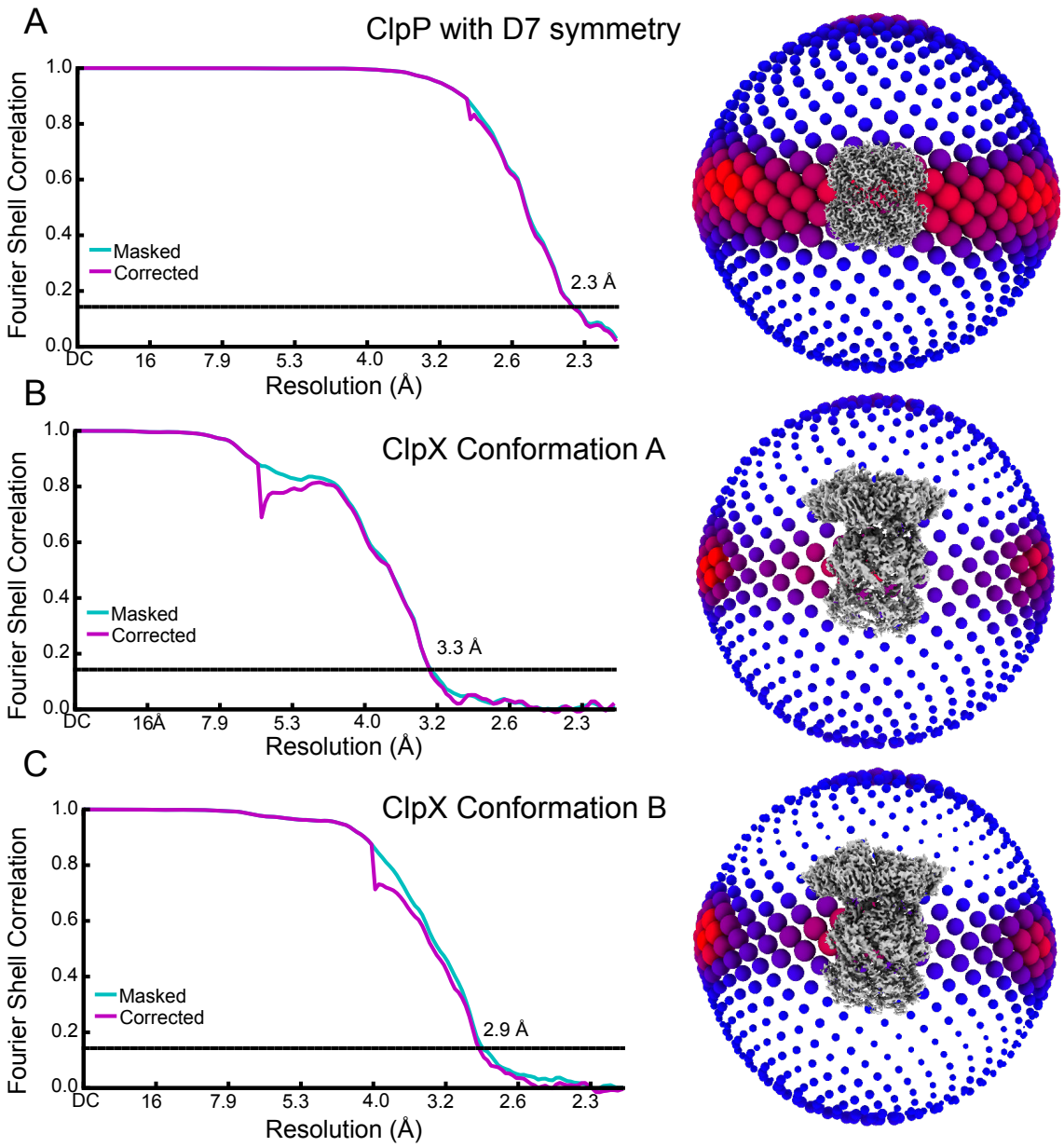

Figure 1 – Figure Supplement 3. Cryo-EM map validation. (A to C) Fourier Shell Correlation (FSC) plots (left) and orientation distribution (right). Resolution values reported are for FSC=0.143.

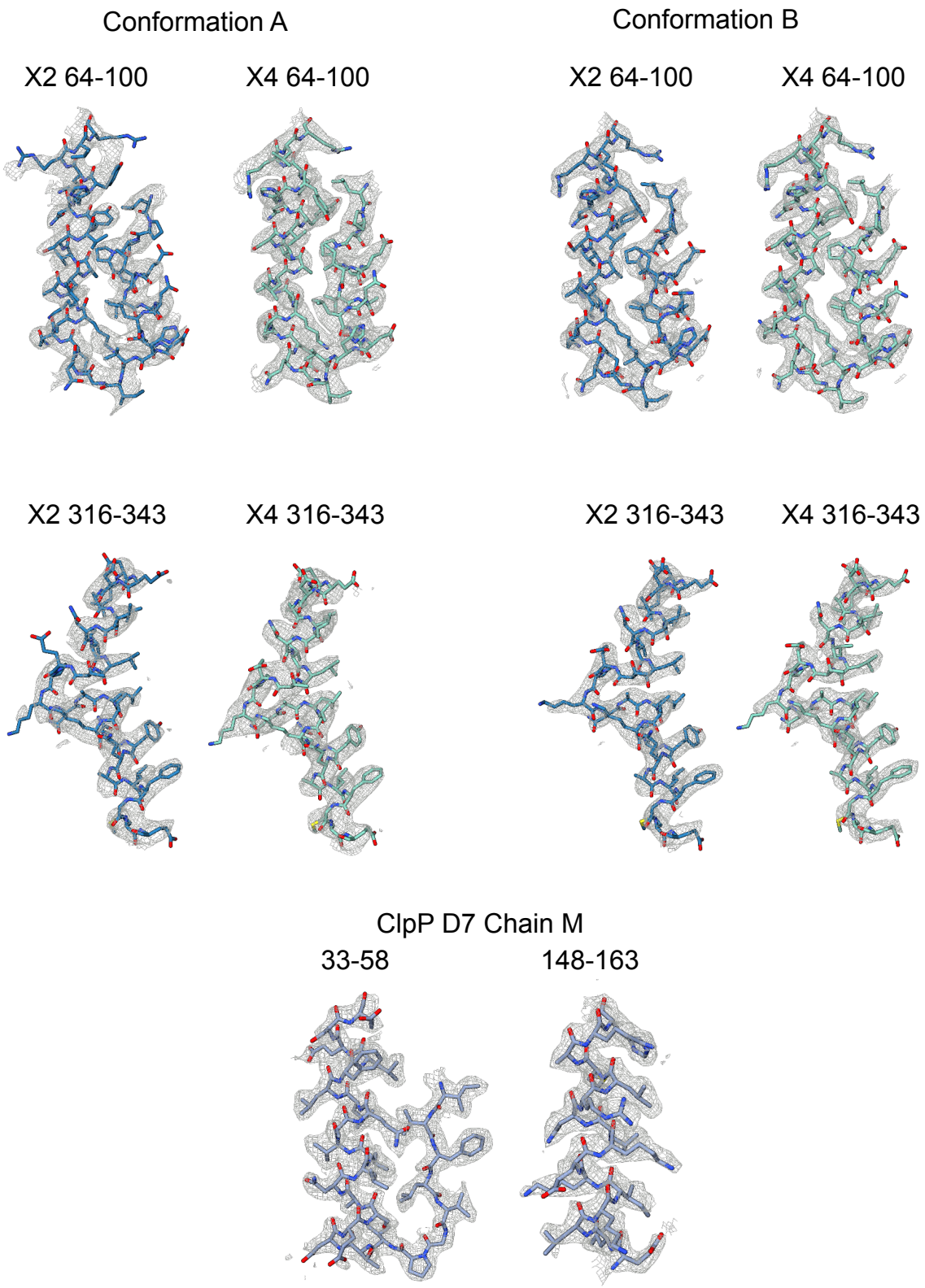

Figure 1 – Figure Supplement 4. Examples of regions of the atomic models built into the experimental cryo-EM maps.

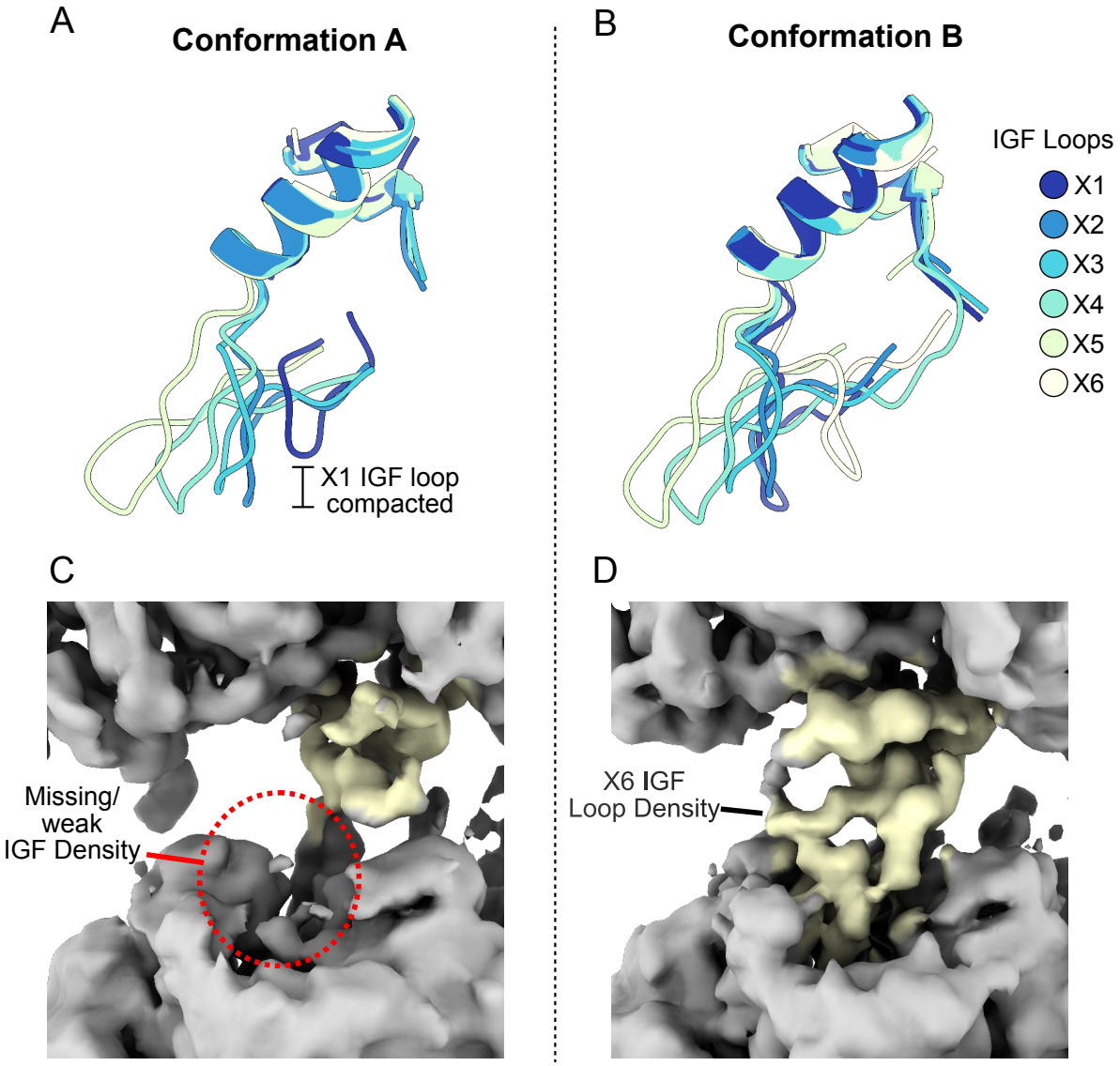

Figure 2 - Figure Supplement 1. IGF loop flexibility. (A and B) Large domains of ClpX were aligned and models for the IGF loops are shown. (C and D) Unsharpened density map for Conformations A and B looking at protomer X6.

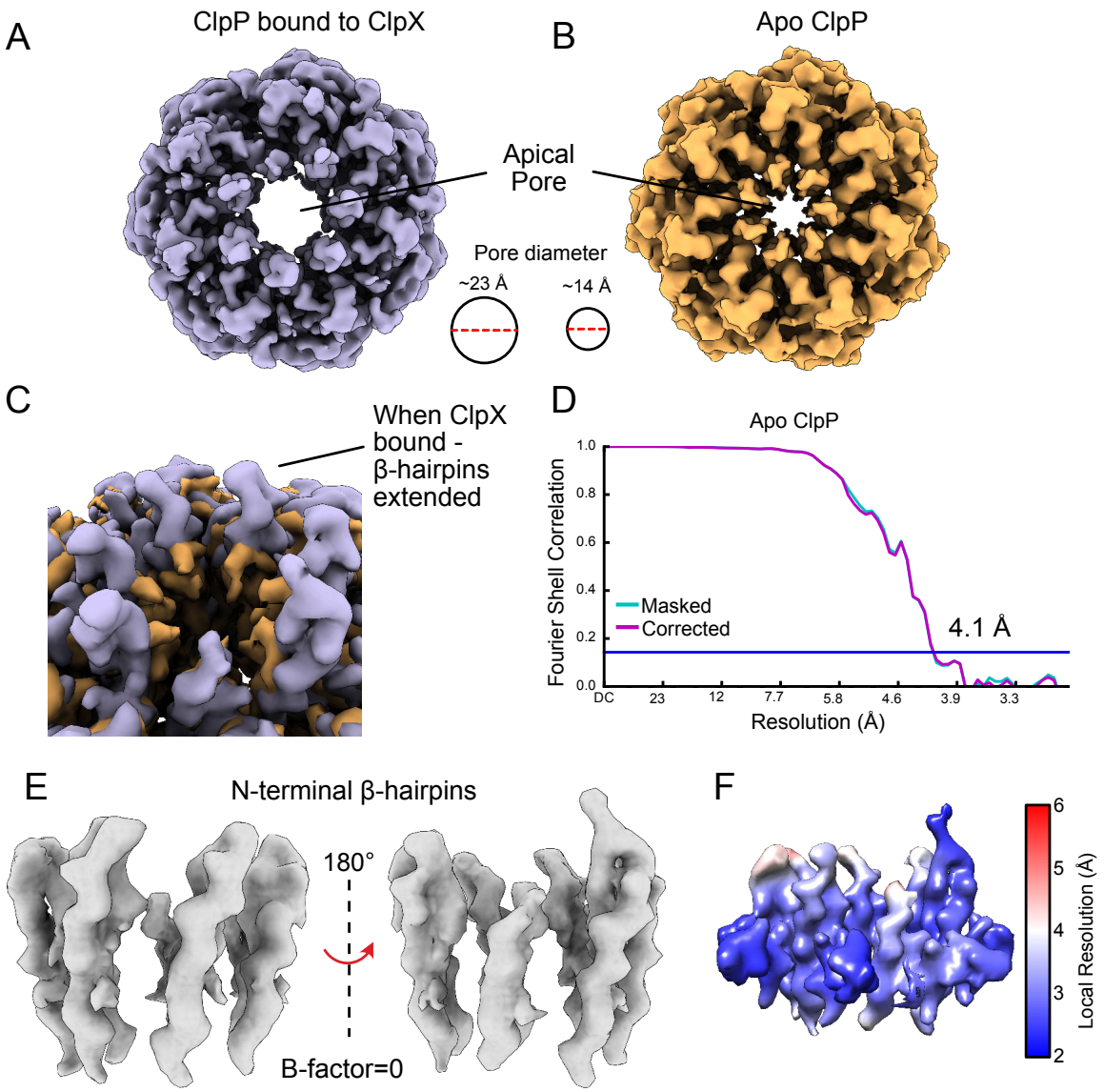

Figure 2 - Figure Supplement 2. The ClpP apical loops extend upwards from the ring surface. (A) Unsharpened density map of the ClpP N-terminal β-hairpins when bound to ClpX. (B) Cryo-EM map of apo ClpP from *N. meningitidis* showing that the apical loops no longer extend "up". (C) ClpX-bound and apo forms of ClpP overlaid. There is no noticeable density for the turn of the ClpP N-terminal β-hairpin in the apo form, and the β-hairpins point inwards, constricting the axial pore of ClpP. (D) Fourier Shell Correlation (FSC) plot for Apo-NmClpP. (E) Closeup view of the N-terminal β-hairpins when bound to ClpX. (F) Density map of the β-hairpins in the ClpXP complex, colored by local resolution.

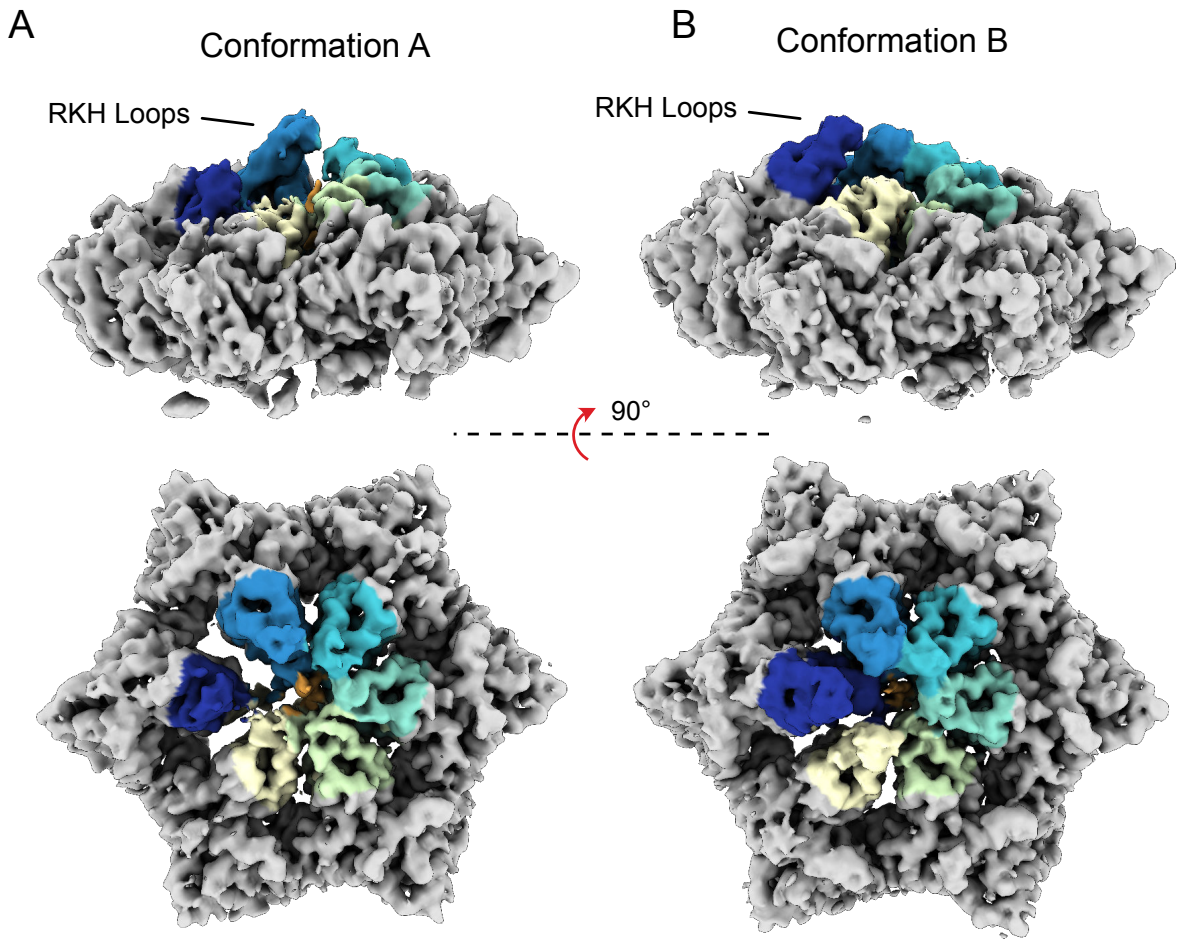

Figure 3 - Figure Supplement 1. RKH loop positions. (A and B) Unsharpened maps for both conformations A and B of ClpX are shown, with RKH loops highlighted in color (coloring done by a radius of 10 Å around residues 220-240).

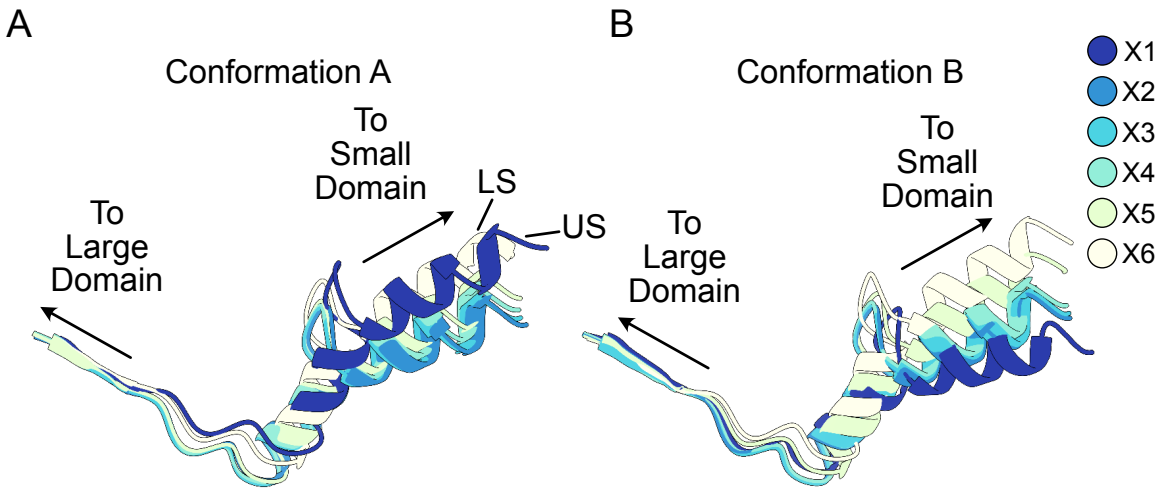

Figure 4 - Figure Supplement 1. Relative orientation between large and small domains of ClpX. (A and B). Residues 308-343 are shown. Note that protomers X1 and X6 in Conformations A and B, respectively, are displaced from substrate. These show among the largest differences in domain orientations.

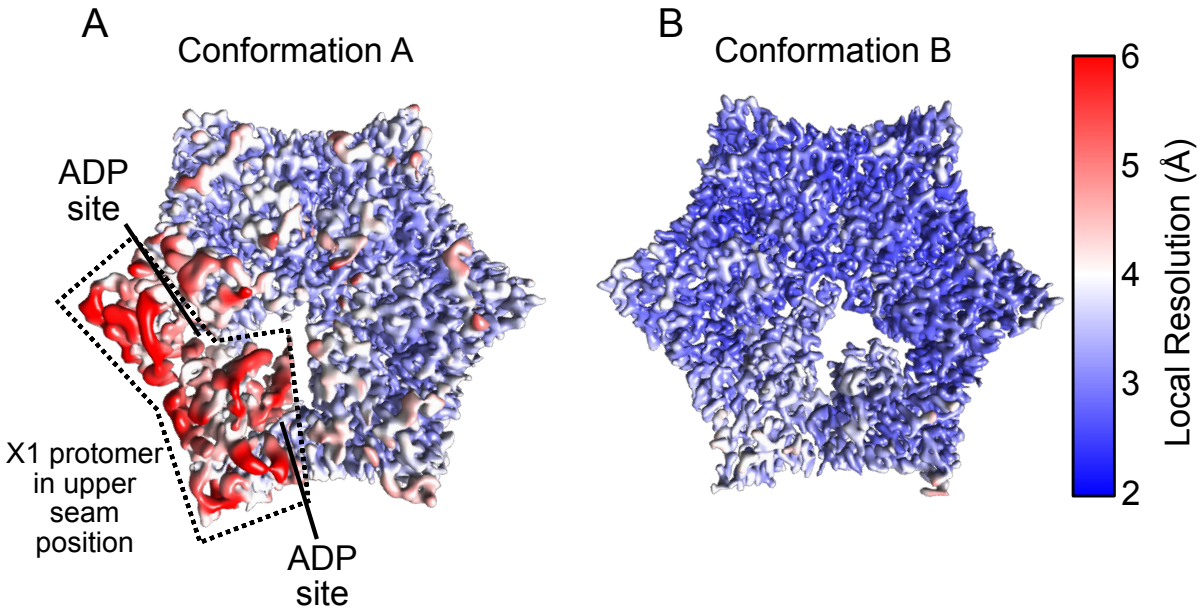

Figure 4 - Figure Supplement 2. Local resolution maps of ClpX. (A and B) Density maps colored by local resolution for Conformations A and B. In Conformation A the US protomer is highlighted with a dashed line.

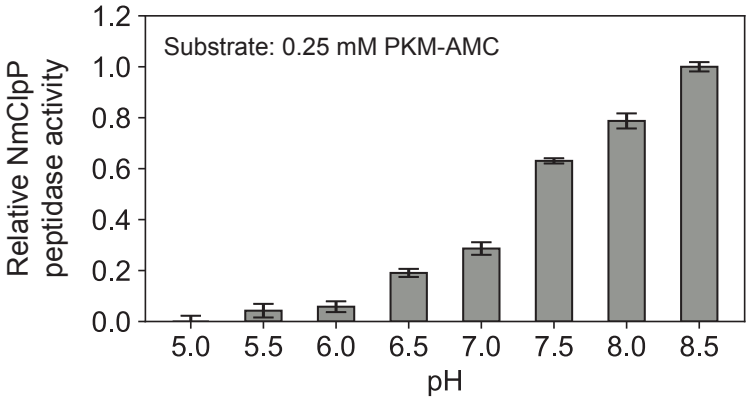

506
507 **Appendix Figure 1.** Peptidase rate measurements of NmClpP as a function of pH, monitored using the fluorogenic
508 substrate PKM-AMC.

509 **Video 1. Overview of the substrate bound ClpXP complex (Conformation B).**

510 **Video 2. Hand-over-hand translocation cycle of the ClpXP complex.** Interpolation between
511 states A → B → A → B. Side and top views of the complex are shown (top), along with the
512 pore-1 loop Tyr153 and substrate (bottom left) as well as IGF loops (bottom right).

513 **Video 3. ClpX precession on the ClpP apical surface.** Repeated interpolation between states
514 reveals a precession of the ClpX ring as its IGF loops are placed successively in different ClpP
515 binding sites. The position of the empty binding pocket on ClpP undergoes a complete cycle
516 around the complex for every 60º rotation of the ClpX ring relative to the ClpP ring.

517

518 **Supplementary File 1.** Cryo-EM data acquisition, processing, model statistics, and data
519 deposition. (A) CryoEM data acquisition and image processing. (B) Map and Model statistics.
520 (C) Residues excluded in atomic models. (D) Deposited maps and associated coordinate files.

521

522 **Materials and Methods:**

523 ***Plasmids and constructs*** Codon-optimized genes encoding NmClpX (Uniprot entry: Q9JYY3)
524 bearing an N-terminal His_6-TEV affinity tag and ClpP (Uniprot entry: Q9JZ38) with an N-
525 terminal His_6-SUMO tag were synthesized by GenScript (Piscataway, NJ, USA) and cloned into
526 the NdeI and BamHI sites of pET28a+ (Novagen, Madison, WI, USA). Point mutations were
527 introduced with the Quikchange mutagenesis method (Agilent, Santa Clara, CA, USA).

528 ***Expression and purification of NmClpP and NmClpX*** Transformed Codon+ *E. coli* BL21(DE3)
529 cells were grown in LB media at 37 °C. Protein over-expression was induced by addition of 0.2
530 mM IPTG at OD_{600}=1.0 and was allowed to proceed overnight at 18 °C. Cells were lysed in
531 buffer containing 50 mM Tris, 300 KCl, 10 mM imidazole, 10% glycerol, pH 7.0 and NmClpP

532 and NmClpX proteins purified by Ni-affinity chromatography [HisTrap HP (GE)] in lysis buffer.
533 Bound proteins were eluted from the Ni column by increasing the imidazole concentration to 500
534 mM. The affinity tag was removed by the addition of TEV (for ClpX) or Ulp1 (for ClpP)
535 protease followed by dialysis against lysis/wash buffer that included 5 mM DTT. Following a
536 reverse Ni-affinity chromatography step, the flow-through, free from the cleaved tag and other
537 impurities, was concentrated with an Amicon Ultra-15 50K MWCO (Millipore) concentrator and
538 subjected to size exclusion chromatography (SEC) with a Superdex 200 Increase 10/300 (GE)
539 column in SEC buffer (50 mM imidazole, 100 mM KCl, 5 mM DTT, pH 7.0). Fractions
540 corresponding to NmClpX and NmClpP were pooled and stored at 4 °C in the SEC buffer until
541 further use. Salts containing magnesium were avoided during the purification of NmClpX to
542 prevent protein aggregation. Protein concentrations were determined in 8 M GdnCl using
543 extinction coefficient values (7450 M^{-1} cm^{-1} for ClpP, 8940 M^{-1} cm^{-1} for ClpX) determined with
544 ExPASy's ProtParam (69).
545 ***Expression and purification of GFP-SsrA.*** Green fluorescent protein (GFP) bearing an 11-
546 residue SsrA degradation tag at its carboxyl terminus and a non-cleavable N-terminal His×6 tag
547 was purified by Ni affinity chromatography followed by SEC on a HiLoad 16/60 Superdex 75 pg
548 column (GE).
549 ***Peptidase rate measurements of NmClpP as a function of pH.*** The peptidase activity of
550 NmClpP was measured at 37 ºC with Acetyl-L-Pro-L-Lys-L-Met bearing a C-terminal
551 fluorogenic 7-amino-4-methylcoumarin group (PKM-AMC) as substrate. The reaction was
552 followed with a Synergy Neo2 96-well microplate reader making a measurement every 21
553 seconds for 60 minutes at λ_{ex}: 355 nm, λ_{em}: 460 nm. Each well contained 1 μM NmClpP
554 (monomer concentration), 250 μM PKM-AMC, 50 mM citrate, 50 mM phosphate, 50 mM Tris,

555 100 mM KCl in a total volume of 100 μL adjusted to the appropriate pH. Activities are derived
556 from initial rates extracted and analyzed using a python script written in-house. Standard errors
557 are calculated from repeating each reaction in triplicate.

558 ***GFP-SsrA degradation assays.*** Degradation of 1 μM samples of GFP-SsrA was followed by the
559 loss of GFP fluorescence (λ_{ex}: 480 nm, λ_{em}: 508 nm) with a Synergy Neo2 96-well microplate
560 reader at 25 °C. The wells included an ATP-regeneration system (70) that contained 1.5 mM
561 phosphoenolpyruvate, 0.2 mM NADH, 40 μg/mL pyruvate kinase, 40 μg/mL lactate
562 dehydrogenase, and 2 mM MgATP at pH 8.2. In some assays solutions also contained WT
563 NmClpX at 0.5 μM concentration (hexamer) and/or WT ClpP at a 0.25 μM concentration
564 (tetradecamer), as indicated in Figure 1B. All assays were performed in triplicate.

565 ***Preparation of samples for cryo-EM.*** A 1 mL mixture containing 10 μM (tetradecamer)
566 NmClpP and 20 μM NmClpX together with 200 μM GFP-SsrA was incubated with 20 mM
567 MgATP for 10 minutes at room temperature. This mixture was applied to a Superdex 200
568 Increase 10/300 (GE) column equilibrated with 50 mM bicine, 100 mM KCl, 2 mM MgATP, pH
569 adjusted to 8.2 at room temperature (equivalent to pH 8.5 at 4 °C – see Appendix Figure 1), as
570 the running buffer. Following SEC, a 0.5 mL fraction (denoted with a * in Figure 1 – Figure
571 Supplement 1) containing doubly capped ClpXP bound to GFP-SsrA was supplemented with 20
572 μM GFP-SsrA and vitrified immediately without the addition of any cross-linking agent or
573 detergent.

574 ***Sample vitrification.*** 2.5 μL of the sample mixtures were applied to nanofabricated holey gold
575 grids (71–73) with a hole size of ~1 μm, that had been glow discharged in air for 15 seconds.
576 Grids were blotted on both sides using a FEI Vitrobot mark III for 15 seconds at 4 °C and ~100%
577 relative humidity before freezing in a liquid ethane/propane mixture (74).

578 ***Electron Microscopy:*** NmClpXP was imaged with a Thermo Fisher Scientific Titan Krios G3
579 microscope operating at 300 kV and equipped with a FEI Falcon III DDD camera. Structures
580 were calculated from counting mode movies consisting of 30 frames, obtained over a 60 second
581 exposure with defocuses ranging from 0.9 to 1.7 µm. Movies were at a nominal magnification of
582 75000× corresponding to a calibrated pixel size of 1.06 Å and with an exposure of 0.8
583 electrons/pixel/s, giving a total exposure of 43 electrons/Å^2. 2680 movies were collected using
584 the microscope's *EPU* software. The Apo-NmClpP structure (with no ClpX or GFP present) was
585 calculated from data obtained using a FEI Tecnai F20 electron microscope operating at 200 kV
586 and equipped with a Gatan K2 Summit direct detector device camera. Movies consisting of 30
587 frames over a 15 second exposure were obtained with defocuses ranging from 1.7 to 2.9 µm.
588 Movies were collected in counting mode at a nominal magnification of 25000× corresponding to
589 a calibrated pixel size of 1.45 Å and with an exposure of 5 electrons/pixel/s, and a total exposure
590 of 35 electrons/Å^2. 122 movies were collected using Digital Micrograph software.
591 ***EM image analysis:*** Patch based whole frame alignment and exposure weighting was performed
592 in *cryoSPARC* v2 (55) with a 10×10 grid and the resulting averages of frames were used for
593 patch based contrast transfer function (CTF) determination. Templates for particle selection were
594 generated by 2D classification of manually selected particles. Particle images were extracted in
595 300×300-pixel boxes for further analysis. *Ab inito* map calculation was performed on a random
596 subset of 30,000 particle images, generating an initial map showing density for the complex of a
597 ClpP tetradecamer bound to two ClpX hexamers. A single round of 2D classification was used to
598 remove images of damaged particles and other contaminants from a dataset of 466,549 particle
599 images, with selected classes leaving 377,234 particle images for further analysis. Homogeneous

600 refinement of these particle images using D7 symmetry yielded a map of the complex, with good
601 density for only the ClpP portion, at 2.3 Å resolution.

602 To improve the density of the ClpX portion of the map, a round of *Ab initio* classification
603 was performed using three classes, of which two classes containing 289,144 particle images had
604 good density for ClpX, with the remaining class containing mostly density for ClpP. Refinement
605 of these particle images with C1 symmetry resulted in a map of the ClpXP complex at a nominal
606 resolution of 2.8 Å, but with poorly defined density for much of ClpX. To improve the
607 interpretability of the map in the ClpX region, local refinement was performed with a mask
608 around the six ClpX subunits without performing signal subtraction for ClpP. This refinement
609 greatly improved the map in the ClpX region, while blurring the density at the distal ClpP ring
610 (indicative of flexibility between ClpX and ClpP). However, density for two of the ClpX
611 subunits remained fragmented and at lower resolution. To help resolve the heterogeneity of this
612 region "3D variability analysis" was performed, which utilizes principle component analysis to
613 separate conformations. Clustering was performed along three eigenvectors. Two clusters were
614 identified along a single eigenvector corresponding to two conformations of ClpX bound to
615 substrate. From the trajectory identified, the two endpoints were used to seed a heterogeneous
616 classification in which the O-EM learning rate was reduced 10-fold to preserve the original
617 character of the seeds yielding two classes split ~ 40%:60% with 110,696 and 178,448 particle
618 images for Conformations A and B respectively. Subsequent non-uniform refinement yielded
619 maps at 3.3 Å and 2.9 Å respectively, which were then used for model building.

620 For Apo-NmClpP the same preprocessing steps were applied as described above, and
621 100,132 particle images were extracted in 160×160-pixel boxes for further analysis. Rounds of

622 2D classification and *ab initio* classification led to a subset of 50,400 particle images that were
623 used to refined a map to 4.1 Å resolution.
624 ***Atomic Model Building and Refinement:*** To model NmClpP, the crystal structure of NmClpP
625 (PDBID: 5DKP) (56) was rigidly fit with UCSF Chimera (75) into the 2.3 Å D7 symmetric map,
626 followed by relaxation with Rosetta using the density map as an additional term in the scoring
627 function (76), and utilizing D7 non crystallographic symmetry. The best scoring model was then
628 rigidly fit into the C1 symmetry focussed maps for Conformation A and B. Visual inspection and
629 real space refinement in *Coot* (77) was then used to better fit the model into the density where it
630 deviated from the ideal symmetry version, specifically in areas where ClpX contacted ClpP, and
631 the apical loops (N-terminal β-hairpins).
632 For NmClpX, Phyre2 (78) was used to perform one-to-one threading onto the previous
633 crystal structure of ClpX from *E. coli* (PDBID 3HWS chain A) (48). A single chain was then
634 rigidly docked into the X3 position of the 2.9 Å map, and real space refinement and *Ab initio*
635 model building of regions that poorly fit the density, as well as for regions missing from the
636 homology model was performed in *Coot* (77). This model was then relaxed with Rosetta (76),
637 and rigidly fit into the density for the other five ClpX protomers. Iterative rounds of real space
638 refinement and *Ab initio* model building in *Coot* (77), relaxation in Rosetta (76), and real space
639 refinement in Phenix (79), were then used to create the final model. To model Conformation A,
640 the model for Conformation B was used as a starting point before iterative rounds of real space
641 refinement and *Ab initio* model building in *Coot*, relaxation in Rosetta, and real space refinement
642 in Phenix. Models were evaluated with Molprobity (80) and EMRinger (81). Figures and movies
643 were generated in UCSF Chimera (75) and UCSF ChimeraX (82), and colors chosen with
644 ColorBrewer (83).

Acknowledgements

We thank Dr. Samir Benlekbir for cryo-EM data collection on the Titan Krios. ZAR and SV were supported by a scholarship and a postdoctoral fellowship from the Canadian Institutes of Health Research, respectively. LEK and JLR were supported by the Canada Research Chairs program. This research was funded by Canadian Institutes of Health Research grants MOP-133408 (LEK), PJT-162186 (JLR), and PJT-148564 (WAH). Titan Krios cryo-EM data were collected at the Toronto High-Resolution High-Throughput cryo-EM facility supported by the Canadian Foundation for Innovation and Ontario Research Fund.

653 **References:**

654 1. A. O. Olivares, T. A. Baker, R. T. Sauer, Mechanistic insights into bacterial AAA+
655 proteases and protein-remodelling machines. *Nat. Rev. Microbiol.* **14**, 33–44 (2016).
656 2. A. L. Goldberg, Protein degradation and protection against misfolded or damaged
657 proteins. *Nature* **426**, 895–899 (2003).
658 3. D. Frees, U. Gerth, H. Ingmer, Clp chaperones and proteases are central in stress survival,
659 virulence and antibiotic resistance of Staphylococcus aureus. *Int. J. Med. Microbiol.* **304**,
660 142–149 (2014).
661 4. C. M. Pickart, R. E. Cohen, Proteasomes and their kin: proteases in the machine age. *Nat.*
662 *Rev. Mol. Cell Biol.* **5**, 177–187 (2004).
663 5. V. Bhandari, K. S. Wong, J. L. Zhou, M. F. Mabanglo, R. A. Batey, W. A. Houry, The
664 Role of ClpP Protease in Bacterial Pathogenesis and Human Diseases. *ACS Chem. Biol.*
665 **13**, 1413–1425 (2018).
666 6. T. A. Baker, R. T. Sauer, ClpXP, an ATP-powered unfolding and protein-degradation
667 machine. *Biochim. Biophys. Acta* **1823**, 15–28 (2012).
668 7. T. Böttcher, S. A. Sieber, β-Lactones as Privileged Structures for the Active-Site Labeling
669 of Versatile Bacterial Enzyme Classes. *Angew. Chem. Int. Ed.* **47**, 4600–4603 (2008).
670 8. M. W. Hackl, M. Lakemeyer, M. Dahmen, M. Glaser, A. Pahl, K. Lorenz-Baath, T.
671 Menzel, S. Sievers, T. Böttcher, I. Antes, H. Waldmann, S. A. Sieber, Phenyl Esters Are
672 Potent Inhibitors of Caseinolytic Protease P and Reveal a Stereogenic Switch for
673 Deoligomerization. *J. Am. Chem. Soc.* **137**, 8475–8483 (2015).
674 9. M. Lakemeyer, E. Bertosin, F. Möller, D. Balogh, R. Strasser, H. Dietz, S. A. Sieber,
675 Tailored peptide phenyl esters block ClpXP proteolysis by an unusual breakdown into a

676 heptamer-hexamer assembly. *Angew. Chemie Int. Ed.* **0** (2019).

677 10. W. Gao, *et al.*, The Cyclic Peptide Ecumicin Targeting ClpC1 Is Active
678 againstMycobacterium tuberculosis In Vivo. *Antimicrob. Agents Chemother.* **59**, 880
679 (2015).

680 11. E. Gavrish, *et al.*, Lassomycin, a Ribosomally Synthesized Cyclic Peptide, Kills
681 Mycobacterium tuberculosis by Targeting the ATP-Dependent Protease ClpC1P1P2.
682 *Chem. Biol.* **21**, 509–518 (2014).

683 12. M. P. Choules, *et al.*, Rufomycin Targets ClpC1 Proteolysis in Mycobacterium
684 tuberculosis and M. abscessus. *Antimicrob. Agents Chemother.* **63**, e02204-18 (2019).

685 13. C. Fetzer, V. S. Korotkov, R. Thänert, K. M. Lee, M. Neuenschwander, J. P. von Kries, E.
686 Medina, S. A. Sieber, A Chemical Disruptor of the ClpX Chaperone Complex Attenuates
687 the Virulence of Multidrug-Resistant Staphylococcus aureus. *Angew. Chemie Int. Ed.* **56**,
688 15746–15750 (2017).

689 14. J. Kirstein, A. Hoffmann, H. Lilie, R. Schmidt, H. Rübsamen-Waigmann, H. Brötz-
690 Oesterhelt, A. Mogk, K. Turgay, The antibiotic ADEP reprogrammes ClpP, switching it
691 from a regulated to an uncontrolled protease. *EMBO Mol. Med.* **1**, 37–49 (2009).

692 15. M. Gersch, K. Famulla, M. Dahmen, C. Göbl, I. Malik, K. Richter, V. S. Korotkov, P.
693 Sass, H. Rübsamen-Schaeff, T. Madl, H. Brötz-Oesterhelt, S. A. Sieber, AAA+
694 chaperones and acyldepsipeptides activate the ClpP protease via conformational control.
695 *Nat. Commun.* **6**, 6320 (2015).

696 16. K. S. Wong, *et al.*, Acyldepsipeptide Analogs Dysregulate Human Mitochondrial ClpP
697 Protease Activity and Cause Apoptotic Cell Death. *Cell Chem. Biol.* **25**, 1017–1030.e9
698 (2018).

699 17. E. Culp, G. D. Wright, Bacterial proteases, untapped antimicrobial drug targets. *J.*
700 *Antibiot. (Tokyo).* **70**, 366–377 (2017).
701 18. I. T. Malik, H. Brotz-Oesterhelt, Conformational control of the bacterial Clp protease by
702 natural product antibiotics. *Nat. Prod. Rep* **34**, 815–831 (2017).
703 19. R. M. Raju, A. L. Goldberg, E. J. Rubin, Bacterial proteolytic complexes as therapeutic
704 targets. *Nat. Rev. Drug Discov.* **11**, 777–789 (2012).
705 20. C. A. Goard, A. D. Schimmer, Mitochondrial matrix proteases as novel therapeutic targets
706 in malignancy. *Oncogene* **33**, 2690 (2013).
707 21. K. S. Wong, W. A. Houry, "Recent Advances in Targeting Human Mitochondrial AAA+
708 Proteases to Develop Novel Cancer Therapeutics" in *Mitochondria in Health and in*
709 *Sickness*, A. Urbani, M. Babu, Eds. (Springer Singapore, 2019), pp. 119–142.
710 22. J. Wang, J. A. Hartling, J. M. Flanagan, The Structure of ClpP at 2.3 A° Resolution
711 Suggests a Model for ATP-Dependent Proteolysis. *Cell* **91**, 447–456 (1997).
712 23. K. Liu, A. Ologbenla, W. A. Houry, Dynamics of the ClpP serine protease: A model for
713 self-compartmentalized proteases. *Crit. Rev. Biochem. Mol. Biol.* **49**, 400–412 (2014).
714 24. F. Förster, P. Unverdorben, P. Śledź, W. Baumeister, Unveiling the Long-Held Secrets of
715 the 26S Proteasome. *Structure* **21**, 1551–1562 (2013).
716 25. E. Kish-Trier, C. P. Hill, Structural Biology of the Proteasome. *Annu. Rev. Biophys.* **42**,
717 29–49 (2013).
718 26. J. Ortega, H. S. Lee, M. R. Maurizi, A. C. Steven, Alternating translocation of protein
719 substrates from both ends of ClpXP protease. *EMBO J.* **21**, 4938–4949 (2002).
720 27. J. Ortega, S. K. Singh, T. Ishikawa, M. R. Maurizi, A. C. Steven, Visualization of
721 Substrate Binding and Translocation by the ATP-Dependent Protease, ClpXP. *Mol. Cell* **6**,

722 1515–1521 (2000).
723 28. M. Kessel, M. R. Maurizi, B. Kim, E. Kocsis, B. L. Trus, S. K. Singh, A. C. Steven,
724 Homology in Structural Organization Between E. coli ClpAP Protease and the Eukaryotic
725 26 S Proteasome. *J. Mol. Biol.* **250**, 587–594 (1995).
726 29. M. E. Lee, T. A. Baker, R. T. Sauer, Control of Substrate Gating and Translocation into
727 ClpP by Channel Residues and ClpX Binding. *J. Mol. Biol.* **399**, 707–718 (2010).
728 30. D. H. S. Li, Y. S. Chung, M. Gloyd, E. Joseph, R. Ghirlando, G. D. Wright, Y. Q. Cheng,
729 M. R. Maurizi, A. Guarne, J. Ortega, Acyldepsipeptide Antibiotics Induce the Formation
730 of a Structured Axial Channel in ClpP: A Model for the ClpX/ClpA-Bound State of ClpP.
731 *Chem. Biol.* **17**, 959–969 (2010).
732 31. G. Effantin, M. R. Maurizi, A. C. Steven, Binding of the ClpA Unfoldase Opens the Axial
733 Gate of ClpP Peptidase. *J. Biol. Chem.* **285**, 14834–14840 (2010).
734 32. Y.-I. Kim, I. Levchenko, K. Fraczkowska, R. V Woodruff, R. T. Sauer, T. A. Baker,
735 Molecular determinants of complex formation between Clp/Hsp100 ATPases and the
736 ClpP peptidase. *Nat. Struct. Biol.* **8**, 230–233 (2001).
737 33. S. A. Joshi, G. L. Hersch, T. A. Baker, R. T. Sauer, Communication between ClpX and
738 ClpP during substrate processing and degradation. *Nat Struct Mol Biol* **11**, 404–411
739 (2004).
740 34. A. J. Amor, K. R. Schmitz, T. A. Baker, R. T. Sauer, Roles of the ClpX IGF loops in ClpP
741 association, dissociation, and protein degradation. *Protein Sci.* **28**, 756–765 (2019).
742 35. A. Gribun, M. S. Kimber, R. Ching, R. Sprangers, K. M. Fiebig, W. A. Houry, The ClpP
743 Double Ring Tetradecameric Protease Exhibits Plastic Ring-Ring Interactions, and the N
744 Termini of Its Subunits Form Flexible Loops That Are Essential for ClpXP and ClpAP

745 Complex Formation. *J. Bio. Chem.* **280**, 16185–16196 (2005).

746 36. L. D. Jennings, J. Bohon, M. R. Chance, S. Licht, The ClpP N-Terminus Coordinates
747 Substrate Access with Protease Active Site Reactivity. *Biochemistry* **47**, 11031–11040
748 (2008).

749 37. A. Martin, T. A. Baker, R. T. Sauer, Diverse Pore Loops of the AAA+ ClpX Machine
750 Mediate Unassisted and Adaptor-Dependent Recognition of ssrA-Tagged Substrates. *Mol.*
751 *Cell* **29**, 441–450 (2008).

752 38. A. Martin, T. A. Baker, R. T. Sauer, Pore loops of the AAA+ ClpX machine grip
753 substrates to drive translocation and unfolding. *Nat Struct Mol Biol* **15**, 1147–1151 (2008).

754 39. N. Monroe, H. Han, P. S. Shen, W. I. Sundquist, C. P. Hill, Structural basis of protein
755 translocation by the Vps4-Vta1 AAA ATPase. *Elife* **6** (2017).

756 40. H. Yu, T. J. Lupoli, A. Kovach, X. Meng, G. Zhao, C. F. Nathan, H. Li, ATP hydrolysis-
757 coupled peptide translocation mechanism of Mycobacterium tuberculosis ClpB. *Proc.*
758 *Natl. Acad. Sci. U. S. A.* **115**, E9560–E9569 (2018).

759 41. A. H. De la Peña, E. A. Goodall, S. N. Gates, G. C. Lander, A. Martin, Substrate-engaged
760 26S proteasome structures reveal mechanisms for ATP-hydrolysis–driven translocation.
761 *Science (80-.).* **362**, eaav0725 (2018).

762 42. M. Shin, A. Asmita, C. Puchades, E. Adjei, R. L. Wiseman, A. W. Karzai, G. C. Lander,
763 Distinct Structural Features of the Lon Protease Drive Conserved Hand-over-Hand
764 Substrate Translocation. *bioRxiv*, 617159 (2019).

765 43. Z. A. Ripstein, R. Huang, R. Augustyniak, L. E. Kay, J. L. Rubinstein, Structure of a
766 AAA+ unfoldase in the process of unfolding substrate. *Elife* **6**, e25754 (2017).

767 44. S. N. Gates, *et al.*, Ratchet-like polypeptide translocation mechanism of the AAA +

768 disaggregase Hsp104. **1052**, 1–13 (2017).

769 45. M. Li, O. Kandror, T. Akopian, P. Dharkar, A. Wlodawer, M. R. Maurizi, A. L. Goldberg,
770 Structure and Functional Properties of the Active Form of the Proteolytic Complex,
771 ClpP1P2, from Mycobacterium tuberculosis. *J. Biol. Chem.* **291**, 7465–7476 (2016).

772 46. S. R. Geiger, T. Bottcher, S. A. Sieber, P. Cramer, A Conformational Switch Underlies
773 ClpP Protease Function. *Angew. Chem. Int. Ed.* **50**, 5749–5752 (2011).

774 47. J. Ishizawa, *et al.*, Mitochondrial ClpP-Mediated Proteolysis Induces Selective Cancer
775 Cell Lethality. *Cancer Cell* (2019)
776 https:/doi.org/https://doi.org/10.1016/j.ccell.2019.03.014.

777 48. S. E. Glynn, A. Martin, A. R. Nager, T. A. Baker, R. T. Sauer, Structures of Asymmetric
778 ClpX Hexamers Reveal Nucleotide-Dependent Motions in a AAA+ Protein-Unfolding
779 Machine. *Cell* **139**, 744–756 (2007).

780 49. M. C. Bewley, V. Graziano, K. Griffin, J. M. Flanagan, The asymmetry in the mature
781 amino-terminus of ClpP facilitates a local symmetry match in ClpAP and ClpXP
782 complexes. *J. Struct. Biol.* **153**, 113–128 (2006).

783 50. F. Beuron, M. R. Maurizi, D. M. Belnap, E. Kocsis, F. P. Booy, M. Kessel, A. C. Steven,
784 At Sixes and Sevens: Characterization of the Symmetry Mismatch of the ClpAP
785 Chaperone-Assisted Protease. *J. Mol. Biol.* **123**, 248–259 (1998).

786 51. P. Majumder, T. Rudack, F. Beck, R. Danev, G. Pfeifer, I. Nagy, W. Baumeister, Cryo-
787 EM structures of the archaeal PAN-proteasome reveal an around-the-ring ATPase cycle.
788 *Proc. Natl. Acad. Sci.* **116**, 534 LP-539 (2019).

789 52. G. L. Hersch, R. E. Burton, D. N. Bolon, T. A. Baker, R. T. Sauer, Asymmetric
790 Interactions of ATP with the AAA+ ClpX6 Unfoldase: Allosteric Control of a Protein

791 Machine. *Cell* **121**, 1017–1027 (2005).

792 53. R. Grimaud, M. Kessel, F. Beuron, A. C. Steven, M. R. Maurizi, Enzymatic and Structural
793 Similarities between the Escherichia coli ATP-dependent Proteases, ClpXP and ClpAP. *J.*
794 *Biol. Chem.* **273**, 12476–12481 (1998).

795 54. J. M. Jones, D. J. Welty, H. Nakai, Versatile Action of Escherichia coli ClpXP as Protease
796 or Molecular Chaperone for Bacteriophage Mu Transposition. *J. Biol. Chem.* **273**, 459–
797 465 (1998).

798 55. A. Punjani, J. L. Rubinstein, D. J. Fleet, M. A. Brubaker, cryoSPARC: algorithms for
799 rapid unsupervised cryo-EM structure determination. *Nat. Methods* **14**, 290–+ (2017).

800 56. J. D. Goodreid, J. Janetzko, J. P. Santa Maria, K. S. Wong, E. Leung, B. T. Eger, S.
801 Bryson, E. F. Pai, S. D. Gray-Owen, S. Walker, W. A. Houry, R. A. Batey, Development
802 and Characterization of Potent Cyclic Acyldepsipeptide Analogues with Increased
803 Antimicrobial Activity. *J. Med. Chem.* **59**, 624–646 (2016).

804 57. A. Martin, T. A. Baker, R. T. Sauer, Distinct static and dynamic interactions control
805 ATPase-Peptidase communication in a AAA plus protease. *Mol. Cell* **27**, 41–52 (2007).

806 58. J. Ortega, H. S. Lee, M. R. Maurizi, A. C. Steven, ClpA and ClpX ATPases bind
807 simultaneously to opposite ends of ClpP peptidase to form active hybrid complexes. *J.*
808 *Struct. Biol.* **146**, 217–226 (2004).

809 59. S. K. Singh, R. Grimaud, J. R. Hoskins, S. Wickner, M. R. Maurizi, Unfolding and
810 internalization of proteins by the ATP-dependent proteases ClpXP and ClpAP. *Proc. Natl.*
811 *Acad. Sci.* **97**, 8898 LP-8903 (2000).

812 60. A. Martin, T. A. Baker, R. T. Sauer, Distinct Static and Dynamic Interactions Control
813 ATPase-Peptidase Communication in a AAA+ Protease. *Mol. Cell* **27**, 41–52 (2007).

814 61. C. M. Farrell, T. A. Baker, R. T. Sauer, Altered Specificity of a AAA+ Protease. *Mol. Cell*
815 **25**, 161–166 (2007).
816 62. S. M. Siddiqui, R. T. Sauer, T. A. Baker, Role of the processing pore of the ClpX AAA+
817 ATPase in the recognition and engagement of specific protein substrates. *Genes Dev.* **18**,
818 369–374 (2004).
819 63. R. Augustyniak, L. E. Kay, Cotranslocational processing of the protein substrate
820 calmodulin by an AAA+ unfoldase occurs via unfolding and refolding intermediates.
821 *Proc. Natl. Acad. Sci.* **115**, E4786 LP-E4795 (2018).
822 64. C. Gatsogiannis, D. Balogh, F. Merino, S. A. Sieber, S. Raunser, Cryo-EM structure of the
823 ClpXP protein degradation machinery. *bioRxiv*, 638692 (2019).
824 65. X. Fei, T. A. Bell, S. Jenni, B. M. Stinson, T. A. Baker, S. C. Harrison, R. T. Sauer,
825 Structures of the ATP-fueled ClpXP proteolytic machine bound to protein substrate.
826 *bioRxiv*, 704999 (2019).
827 66. E. J. Enemark, L. Joshua-Tor, Mechanism of DNA translocation in a replicative
828 hexameric helicase. *Nature* **442**, 270–275 (2006).
829 67. R. Huang, Z. a Ripstein, R. Augustyniak, M. Lazniewski, K. Ginalski, L. E. Kay, J. L.
830 Rubinstein, Unfolding the mechanism of the AAA+ unfoldase VAT by a combined cryo-
831 EM, solution NMR study. *Proc. Natl. Acad. Sci. U. S. A.* (2016)
832 https:/doi.org/10.1073/pnas.1603980113.
833 68. A. Martin, T. A. Baker, R. T. Sauer, Rebuilt AAA + motors reveal operating principles for
834 ATP-fuelled machines. *Nature* **437**, 1115–1120 (2005).
835 69. E. Gasteiger, C. Hoogland, A. Gattiker, S. Duvaud, M. R. Wilkins, R. D. Appel, A.
836 Bairoch, "Protein Identification and Analysis Tools on the ExPASy Server" in *The*

837 *Proteomics Protocols Handbook*, J. M. Walker, Ed. (Humana Press, 2005), pp. 571–607.
838 70. J. G. B. T.-M. in E. Nørby, "[11] Coupled assay of Na+,K+-ATPase activity" in
839 *Biomembranes Part P: ATP-Driven Pumps and Related Transport: The Na,K-Pump*,
840 (Academic Press, 1988), pp. 116–119.
841 71. C. R. Marr, S. Benlekbir, J. L. Rubinstein, Fabrication of carbon films with ~500nm holes
842 for cryo-EM with a direct detector device. *J. Struct. Biol.* **185**, 42–47 (2014).
843 72. C. J. Russo, L. A. Passmore, Ultrastable gold subtrates for electron cryomicroscopy.
844 *Science (80-.).* **346**, 1377–1380 (2014).
845 73. J. R. Meyerson, P. Rao, J. Kumar, S. Chittori, S. Banerjee, J. Pierson, M. L. Mayer, S.
846 Subramaniam, Self-assembled monolayers improve protein distribution on holey carbon
847 cryo-EM supports. *Sci. Rep.* **4**, 7084 (2014).
848 74. W. F. Tivol, A. Briegel, G. J. Jensen, An improved cryogen for plunge freezing. *Microsc.*
849 *Microanal.* **14**, 375–379 (2008).
850 75. E. F. Pettersen, T. D. Goddard, C. C. Huang, G. S. Couch, D. M. Greenblatt, E. C. Meng,
851 T. E. Ferrin, UCSF Chimera—A visualization system for exploratory research and
852 analysis. *J. Comput. Chem.* **25**, 1605–1612 (2004).
853 76. R. Y. R. Wang, M. Kudryashev, X. Li, E. H. Egelman, M. Basler, Y. Cheng, D. Baker, F.
854 Dimaio, De novo protein structure determination from near-atomic-resolution cryo-EM
855 maps. *Nat. Methods* **12**, 335–338 (2015).
856 77. P. Emsley, K. Cowtan, Coot: model-building tools for molecular graphics. *Acta*
857 *Crystallogr. Sect. D* **60**, 2126–2132 (2004).
858 78. L. A. Kelley, S. Mezulis, C. M. Yates, M. N. Wass, M. J. E. Sternberg, The Phyre2 web
859 portal for protein modeling, prediction and analysis. *Nat. Protoc.* **10**, 845 (2015).

79. P. D. Adams, *et al.*, PHENIX: a comprehensive Python-based system for macromolecular structure solution. *Acta Crystallogr. Sect. D* **66**, 213–221 (2010).

80. V. B. Chen, W. B. Arendall III, J. J. Headd, D. A. Keedy, R. M. Immormino, G. J. Kapral, L. W. Murray, J. S. Richardson, D. C. Richardson, MolProbity: all-atom structure validation for macromolecular crystallography. *Acta Crystallogr. Sect. D* **66**, 12–21 (2010).

81. B. A. Barad, N. Echols, R. Y.-R. Wang, Y. Cheng, F. DiMaio, P. D. Adams, J. S. Fraser, EMRinger: side chain–directed model and map validation for 3D cryo-electron microscopy. *Nat. Methods* **12**, 943 (2015).

82. T. D. Goddard, C. C. Huang, E. C. Meng, E. F. Pettersen, G. S. Couch, J. H. Morris, T. E. Ferrin, UCSF ChimeraX: Meeting modern challenges in visualization and analysis. *Protein Sci.* **27**, 14–25 (2018).

83. M. Harrower, C. A. Brewer, ColorBrewer.org: An Online Tool for Selecting Colour Schemes for Maps. *Cartogr. J.* **40**, 27–37 (2003).